sustainability

MDPI

Article

Green-Synthesized Ag/Zn Nanocomposites from *Chlorella vulgaris* Polar Extract: Sustainable Photocatalytic Water Remediation and Kinetic Modeling

Federico Zedda [1,2], Federico Atzori [1,2], Silvia Casu [1,2], Agnieszka Sidorowicz [1,2,3], Giacomo Fais [1,2], Francesco Desogus [1], Roberta Licheri [1,*], Stefania Porcu [4], Giacomo Cao [1,2], Giovanni Antonio Lutzu [5] and Alessandro Concas [1,2,*]

[1] Department of Mechanical, Chemical and Materials Engineering, University of Cagliari, Via Marengo 2, 09123 Cagliari, Italy; federico.zedda@unica.it (F.Z.); federico.atzori@unica.it (F.A.); silvia.casu3@unica.it (S.C.); agnieszka.sidorowicz@tuwien.ac.at (A.S.); giacomo.fais@unica.it (G.F.); francesco.desogus2@unica.it (F.D.); giacomo.cao@unica.it (G.C.)
[2] Interdepartmental Centre of Environmental Science and Engineering (CINSA), University of Cagliari, Via San Giorgio 12, 09124 Cagliari, Italy
[3] Institute of Materials Chemistry, Technische Universität Wien, Getreidemarkt 9/BC, 1060 Vienna, Austria
[4] Department of Physics, University of Cagliari, Cittadella Universitaria di Monserrato, 09042 Cagliari, Italy; stefania.porcu@dsf.unica.it
[5] Teregroup Srl, Via David Livingstone 37, 41123 Modena, Italy; gianni.lutzu@teregroup.net
* Correspondence: roberta.licheri@unica.it (R.L.); alessandro.concas@unica.it (A.C.)

Abstract

The growing demand for sustainable water treatment technologies requires photocatalysts that combine low environmental impact, energy efficiency, and mechanistic robustness. In this work, Ag/Zn nanocomposites were green-synthesized using *Chlorella vulgaris* polar extract as a bio-mediated reducing and stabilizing agent, eliminating hazardous reagents and high-energy processing steps. Structural characterization (XRD, FTIR, SEM, UV–Vis) confirmed the coexistence of crystalline wurtzite ZnO with metallic Ag and Ag_2O phases. Photocatalytic activity was evaluated through Congo Red degradation under a sequential dark–light protocol, enabling clear separation of adsorption and photoactivated pathways. During the 60 min dark stage, removal remained limited ($\sim$ 9–11%), consistent with adsorption–desorption equilibration. Upon UV irradiation, a distinct kinetic transition occurred, leading to final removal efficiencies of 44–49% after 180 min. Notably, performance remained stable across the investigated photon flux range, indicating operation beyond a strictly photon-limited regime and highlighting an intrinsically energy-resilient catalytic response. A mechanistic kinetic model integrating reversible adsorption with light-dependent degradation accurately reproduced all experimental profiles ($NRMSE = 3.14\%$) and successfully predicted an independent dark-control experiment without additional fitting. By coupling green synthesis with quantitative kinetic validation, this study proposes a sustainability-oriented framework for designing photocatalysts that align low-impact fabrication with energy-conscious water remediation.

Keywords: green synthesis; Ag/Zn nanocomposites; microalgae-mediated synthesis; emerging contaminants; photocatalytic water treatment; Congo red degradation; sustainable nanomaterials; kinetic modeling

Academic Editors: Jinsong Liang and Longyi Lv

Received: 27 March 2026
Revised: 23 April 2026
Accepted: 26 April 2026
Published: 6 May 2026

https://doi.org/10.3390/su18094607

1. Introduction

Water pollution represents one of the most pressing global sustainability challenges of the 21st century [1–3]. The continuous discharge of persistent organic contaminants into aquatic environments threatens ecosystem integrity, drinking water security, and public health [4]. Among contaminants of emerging concern (CECs), synthetic azo dyes are particularly problematic due to their high chemical stability, low biodegradability, and long-term environmental persistence [5]. Their removal is therefore not merely a technical objective, but a sustainability imperative aligned with global water management and responsible production goals.

Among these pollutants, Congo Red (CR) (Figure 1), a benzidine-based anionic azo dye, is widely recognized as a representative model emerging contaminant [6]. Its complex aromatic structure, together with the presence of azo (–N=N–) linkages, induces a high degree of resistance to conventional biological and physicochemical treatments [7]. Furthermore, its reported mutagenic and carcinogenic effects emphasize the urgency of developing efficient and environmentally responsible remediation strategies [8]. From a methodological standpoint, CR exhibits a strong absorption band in the visible region, enabling accurate spectrophotometric monitoring [9], while its anionic character and relatively large molecular size make it highly sensitive to photocatalyst surface properties and adsorption equilibria [10]. These features make Congo Red an ideal probe molecule for evaluating catalyst–pollutant interactions and surface-mediated degradation mechanisms.

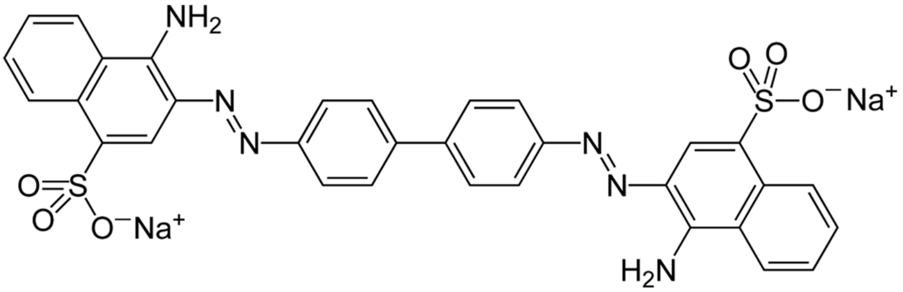

Figure 1. Molecular structure of Congo Red (CR), a benzidine-based anionic azo dye commonly used as a model emerging contaminant in photocatalytic degradation studies.

Advanced oxidation processes (AOPs), and particularly heterogeneous photocatalysis, have emerged as promising technologies for the mineralization of recalcitrant organic pollutants under light irradiation [11,12]. Nanostructured semiconductor photocatalysts offer enhanced surface reactivity, tunable optical properties, and improved charge carrier dynamics, enabling the generation of reactive oxygen species (ROS) capable of oxidizing complex organic molecules [13].

Among these materials, zinc oxide (ZnO) has been extensively investigated due to its wide band gap, strong oxidative potential, high chemical stability, and ability to generate hydroxyl radicals and superoxide species under irradiation [14–16]. The incorporation of noble metals such as silver (Ag) further enhances photocatalytic performance by promoting charge separation and facilitating interfacial electron transfer [17]. In Ag/Zn hybrid systems, silver nanoparticles can act as electron sinks and plasmonic enhancers via localized surface plasmon resonance (LSPR), thereby extending light absorption and reducing electron–hole recombination [18]. As a result, Ag/Zn nanocomposites often exhibit superior activity compared to pristine ZnO [19].

Despite their environmental application, many Zn- and Ag-based nanomaterials are synthesized through energy-intensive procedures involving hazardous chemicals and non-renewable reagents [20,21]. This contradiction reveals a sustainability paradox: materials designed for environmental remediation are frequently produced via environmentally burdensome processes. Addressing this paradox requires rethinking photocatalyst production through eco-design principles that integrate green chemistry, renewable resources, and process efficiency.

In this context, green synthesis strategies based on biological extracts have gained increasing attention as sustainable alternatives to conventional nanoparticle fabrication [22]. Plant- and microalgae-derived extracts can simultaneously act as reducing, stabilizing, and capping agents under mild reaction conditions, minimizing toxic reagents and lowering energy consumption [23]. Beyond reducing environmental impact, biologically mediated synthesis can introduce surface functional groups that influence defect formation, charge transfer processes, and catalytic behavior.

Among biological platforms, *Chlorella vulgaris* represents a particularly attractive candidate [24]. This microalga is rich in proteins, polysaccharides, pigments, and oxygen- and nitrogen-containing metabolites [25] capable of mediating nanoparticle nucleation and growth [26,27]. Importantly, polar extracts derived from microalgal biomass, including streams generated within biorefinery processes, can be valorized as functional reagents for nanomaterial production, thereby transforming residual or low-value biomass into high-value photocatalytic materials. Within a circular economy framework, microalgae-mediated synthesis contributes to sustainability by reducing reliance on synthetic chemical reductants, valorizing renewable biological resources and biorefinery side streams, enabling low-temperature and low-energy processing routes, and potentially coupling wastewater treatment with biomass utilization [28]. Thus, the use of microalgal extracts represents a systemic sustainability strategy that integrates material synthesis, waste valorization, and environmental remediation.

Sustainable water treatment technologies must be evaluated not only in terms of pollutant removal efficiency but also through quantitative performance metrics and reproducible kinetic descriptors [29]. In heterogeneous photocatalysis, degradation kinetics are frequently described using apparent first-order models [30,31]. While such approaches offer mathematical simplicity and facilitate comparison among materials, they inherently condense multiple physicochemical processes into a single lumped rate constant.

Photocatalytic degradation is, however, intrinsically a multistep process [32], particularly in systems where surface chemistry is intentionally modified through green synthesis routes. Biologically derived functional groups can significantly influence adsorption equilibria, interfacial electron transfer, and reactive oxygen species (ROS) mediated reaction pathways. Under these conditions, reducing the system to a pseudo-first-order expression can mask distinct kinetic regimes and obscure the role of surface-mediated phenomena. Introducing a more structured and physically informed kinetic framework enables the discrimination between adsorption-controlled and photoactivation-controlled steps, thereby providing deeper insight into how biosynthetically derived surface features govern catalytic behavior.

By moving beyond purely empirical first-order descriptions and integrating mechanistically oriented kinetic analysis with green material design, it becomes possible to assess not only pollutant removal efficiency but also the fundamental origins of catalytic performance, a necessary step toward the rational development of truly sustainable photocatalytic technologies.

In this study, Ag/Zn nanocomposites were synthesized using polar extracts of *Chlorella vulgaris* and evaluated for the photocatalytic degradation of Congo Red under controlled irradiation conditions. Beyond demonstrating pollutant removal, this work combines eco-designed nanomaterial production, circular resource valorization, and mechanistic kinetic modeling to assess the true sustainability potential of biosynthesized photocatalysts. Through this integrated approach, the present research contributes to the development of low-impact, resource-efficient technologies for water remediation, supporting broader sustainability objectives related to clean water, responsible production, and environmental protection.

2. Materials and Methods

2.1. Preparation of Chlorella vulgaris Polar Extract

The extraction methodology followed a protocol previously reported in our earlier work [33], ensuring methodological consistency with prior investigations.

Chlorella vulgaris (CCALA 902) was cultivated in Bold's Basal Medium (BBM) supplemented with 60 mM $NaHCO_3$ (Merck®, Darmstadt, Germany) as an additional inorganic carbon source. Cultures were maintained under a 12 h light/12 h dark photoperiod using 58 W fluorescent lamps (Osram®, Milan, Italy), providing an incident photon flux of approximately 70 μmol m^{-2} s^{-1}. Agitation at 200 rpm was applied to promote homogeneous cell suspension and nutrient distribution. Growth was monitored spectrophotometrically at 750 nm, and biomass was harvested during the exponential phase ($OD_{750} \approx 0.6$), after approximately 14 days of cultivation.

The collected biomass was recovered by centrifugation at 2000× g, 10 min (Heraeus Megafuge 1.0R, Thermo Fisher Scientific, Milan, Italy), dried at ambient conditions, and subsequently subjected to a lipid-extraction procedure based on the Folch method [34]. Approximately 5 g of dried biomass was dispersed in methanol (100 mL) and kept at 4 °C overnight to facilitate solvent penetration. The suspension was then sonicated for 30 min to promote cell disruption and intracellular component release. A volume of 200 mL of Chloroform (Merck®, Darmstadt, Germany) was added to the mixture, which was then stirred at room temperature for 1 h to enhance extraction efficiency.

After centrifugation (4000 × g, 20 °C, 10 min), phase separation was induced by the addition of 0.88% KCl (Merck®, Darmstadt, Germany) solution. The upper aqueous (polar) and lower organic (apolar) phases were separated carefully. Solvents were removed under reduced pressure using a rotary evaporator (Rotavapor R-210, Buchi, Milan, Italy). Finally, the polar fraction was re-dispersed in 150 mL of MilliQ water (Millipore®, Milan, Italy) and stored at 4 °C until further use in nanoparticle synthesis.

2.2. Catalyst Synthesis

The photocatalytic system was obtained via a sequential two-stage route, as schematically illustrated in Figure 2. Initially, zinc-based nanoparticles (Zn-NPs) were synthesized through a green-assisted precipitation process. Subsequently, these particles were functionalized with silver species to obtain Ag-decorated Zn-based nanoparticles (Ag/Zn-NPs). In both stages, a polar extract derived from *Chlorella vulgaris* was employed as a bio-mediated reducing and stabilizing agent.

The synthetic strategy follows a previously established bio-assisted methodology [33]. In the present study, this validated synthetic methodology was adopted as a reliable foundation for the systematic assessment of photocatalytic activity.

2.2.1. Preparation of Zn-Based Nanoparticles (Zn-NPs)

The synthesis began with the dilution of the *Chlorella vulgaris* polar extract in distilled water at a volumetric ratio of $1:10$ v/v, reaching a total volume of 600 mL. Zinc sulfate heptahydrate ($ZnSO_4 \cdot 7H_2O$, Merck®, Darmstadt, Germany) was then introduced into the solution to achieve a final concentration of 0.1 M (17.25 g in 600 mL). The mixture was magnetically stirred (IKA® RH Digital Magnetic Stirrer, Milan, Italy) at 250 rpm for 15 min to ensure complete homogenization.

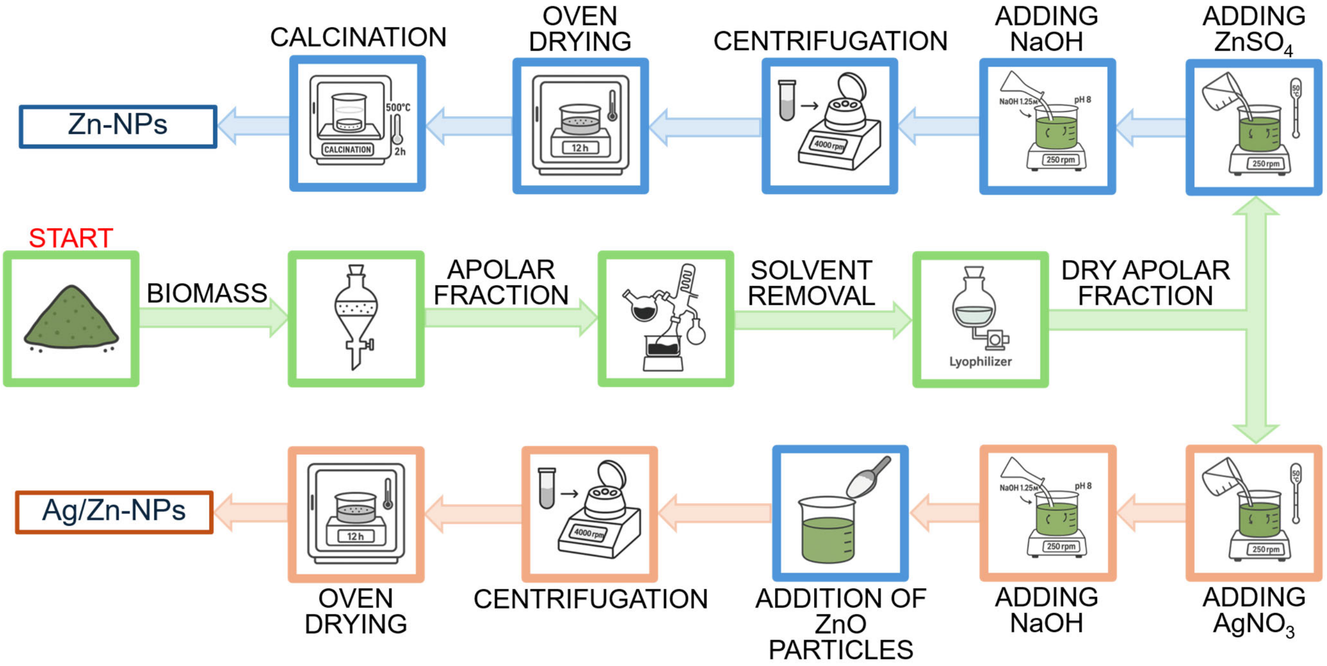

Figure 2. Schematic representation of the green synthesis route for Ag/Zn-NPs nanocomposites using *Chlorella vulgaris* polar extract as a bio-mediated reducing and stabilizing agent. The process involves the initial formation of Zn-based nanoparticles (Zn-NPs), followed by silver functionalization to obtain Ag-decorated Zn-NPs.

The suspension was subsequently heated to 50 °C under continuous agitation. Upon stabilization of the temperature, the pH was carefully increased to 8 by the gradual addition of a 1.25 M $NaOH$ (Merck®, Darmstadt, Germany) solution. The reaction medium was maintained at 50 °C for 90 min to promote controlled nucleation and particle growth.

After the reaction period, the system was allowed to age overnight at room temperature. The solid product was then separated by centrifugation at 4000 rpm for 15 min (Heraeus® Megafuge® 1.0R, Thermo Fisher Scientific, Milan, Italy), thoroughly washed three times with distilled water to eliminate residual species, and dried overnight at 90 °C in a laboratory oven (Heraeus, Thermo Fisher Scientific, Milan, Italy). A final calcination step was performed at 500 °C for 2 h in a muffle furnace (Nabertherm N60/ER, Lilienthal, Germany) to obtain crystalline Zn-NPs.

2.2.2. Preparation of Ag-Decorated Zn-Based Nanoparticles (Ag/Zn-NPs)

For the silver functionalization step, the *Chlorella vulgaris* polar extract was again diluted ($1:10\ v/v$) in distilled water to a total volume of 150 mL. Silver nitrate ($AgNO_3$, Carlo Erba, Milan, Italy) was added to reach a final concentration of 0.1 M (2.55 g in 150 mL), and the obtained solution was then magnetically stirred at 250 rpm for 15 min to ensure proper dissolution and dispersion.

The mixture was heated to 50 °C under continuous stirring. Once thermal equilibrium was achieved, the pH was gradually adjusted to 8 by controlled addition of a 1.25 M $NaOH$ (Merck®, Darmstadt, Germany) solution. The reaction was maintained at 50 °C for 90 min.

After this preliminary stage, 2 g of the previously synthesized Zn-NPs were introduced into the reaction medium. The suspension was then left under static conditions overnight at room temperature to facilitate the deposition and interfacial interaction of silver species onto the Zn-NPs surface.

The resulting composite material was recovered by centrifugation at 4000 rpm for 15 min (Heraeus® Megafuge® 1.0R, Thermo Fisher Scientific, Milan, Italy), washed three times with distilled water, and dried overnight at 90 °C (Heraeus, Thermo Fisher Scientific, Milan, Italy).

2.3. Material Characterization

The crystallographic structure and phase purity of the prepared nanomaterials were investigated by X-ray diffraction (XRD). Diffraction measurements were performed using a Bruker D8 Advance (Bruker, Milan, Italy) diffractometer equipped with Cu Kα radiation ($\lambda = 1.5406$), operating at 40 kV and 30 mA. Patterns were recorded within a 2θ angular interval of 5°–70°, employing a step increment of 0.02°. The obtained diffraction profiles were compared with reference data from the International Centre for Diffraction Data (ICDD) and the Crystallography Open Database (COD) to identify the crystalline phases present. Phase assignment and peak analysis were carried out using Diffrac.Eva software (version 6.1.0.4, Bruker, Milan, Italy).

Surface functional groups associated with the nanoparticles were examined by Fourier Transform Infrared (FTIR) spectroscopy. Spectra were collected using a Jasco FT/IR-6700 (Jasco, Tokyo, Japan) spectrometer equipped with a diamond attenuated total reflectance (ATR) accessory. Powdered samples were directly deposited onto the ATR crystal without additional preparation. Spectral acquisition was performed in the 4000–400 cm^{-1} range with a spectral resolution of 4 cm^{-1}, averaging 64 scans per sample to enhance the signal-to-noise ratio. The spectra were interpreted by assigning characteristic vibrational bands to the corresponding chemical functionalities.

Morphological features and elemental composition were analyzed by scanning electron microscopy (SEM) combined with energy-dispersive X-ray spectroscopy (EDX). Micrographs were obtained using a Hitachi S4000 field-emission gun high-resolution SEM (Hitachi Ltd., Tokyo, Japan) operating at an accelerating voltage of 20 kV. Prior to imaging, samples were coated with an ultrathin ($\sim$ 2 nm) Pt/Au conductive layer to minimize charging and improve image quality. Images were collected at different magnifications and processed using Quartz PCI software (version 7.0, Quartz Imaging Corporation, Vancouver, BC, Canada). Elemental analysis was performed by EDX on selected areas of the samples to determine elemental distribution and relative composition. Spectra were acquired using an UltraDry EDX detector (Thermo Fisher Scientific, Madison, WI, USA) and processed with NSS3 software (version 3, Thermo Fisher Scientific, Madison, WI, USA) to quantify the relative abundance of the main elements.

Optical Properties

Diffuse reflectance spectra were recorded using a JASCO V-770 UV–Vis spectrophotometer (Jasco, Tokyo, Japan) operating in reflectance mode (%R). Measurements were carried out in the wavelength range 800–200 nm, with a data interval of 0.2 nm and a spectral bandwidth of 1.0 nm in the UV–Vis region. A deuterium/tungsten (D2/WI) light source was employed, and baseline correction was applied prior to acquisition.

The reflectance data were converted into absorption-related information using the Kubelka–Munk transformation:

$$F(R_\infty) = \frac{(1-R)^2}{2R} \tag{1}$$

where R is the measured reflectance. For optically thick samples, $F(R_\infty)$ can be considered proportional to the absorption coefficient [35].

The optical band gap energy (E_g) was determined according to the Tauc approach, assuming a direct allowed electronic transition consistent with the wurtzite structure of ZnO [36,37]. In the composite system, this assumption remains valid since Ag incorporation does not modify the direct band-to-band transition of ZnO but rather introduces interfacial states and plasmon-mediated effects without changing the fundamental transition type [38]. The band gap was estimated from the linear region of the $(F(R_\infty)\, h\nu)^2$ versus photon energy $h\nu$ plot by extrapolating the fit to the energy axis [39].

The degree of structural disorder was evaluated through the Urbach energy (E_U), which describes the exponential absorption tail below the fundamental absorption edge [40]. Urbach energy E_U was estimated from the slope of the linear region in the $\ln(F(R_\infty))$ versus photon energy $h\nu$ plot, according to [41]:

$$E_U = \left(\frac{d}{d(h\nu)} \ln(F(R_\infty)) \right)^{-1} \tag{2}$$

2.4. Photocatalytic Experimental Setup

Photocatalytic degradation tests were performed in a batch reactor operated under continuous recirculation, allowing in situ monitoring of dye concentration without manual sampling. The experimental setup consisted of a 1 L glass reactor containing 250 mL of aqueous Congo Red (Merck®, Darmstadt, Germany) solution. The suspension was magnetically stirred throughout the experiment to ensure uniform catalyst dispersion and to avoid mass transfer limitations associated with particle sedimentation.

Irradiation was applied from the top using a UV lamp (Transilluminator M-20V high/medium/low intensity setting, UVP, Upland, CA, USA) with adjustable intensity, positioned 20 cm above the liquid free surface. The lamp emission spectrum (Figure 3) was characterized prior to the experiments and exhibited dominant emission bands in the ultraviolet region, ensuring sufficient photon flux below the ZnO bandgap energy [42]. Three irradiation conditions were defined within the experimental design, corresponding to measured incident intensities of 0.72, 0.89, and 0.99 mW cm^{-2}. The light intensity was quantified at the liquid surface using a calibrated radiometer (Newport 1918-C, Newport Corporation, Andover, MA, USA) and adjusted according to the selected experimental condition.

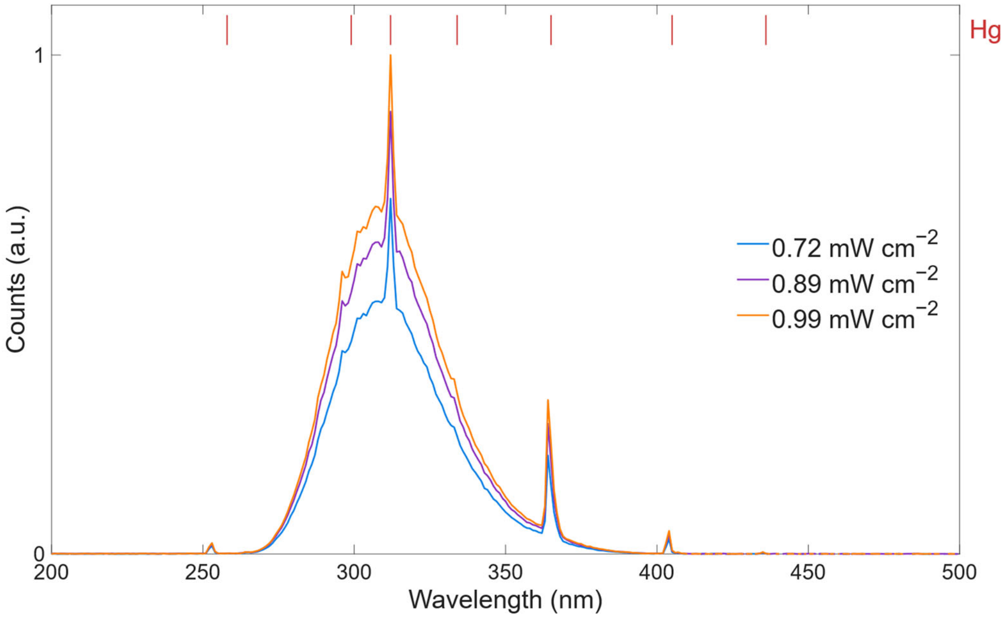

Figure 3. Emission spectra of the Hg lamp measured at three irradiation intensities (0.72, 0.89, and 0.99 mW cm^{-2}), showing the characteristic spectral distribution of the light source used in the photocatalytic experiments.

A closed-loop circulation system enabled continuous spectrophotometric analysis. The suspension was withdrawn from the reactor via a 12 V peristaltic pump and conveyed through polymeric tubing (inner diameter 3 mm, outer diameter 5 mm) to a quartz flow-through cuvette (optical path length: 1 cm) connected to a UV–Vis spectrophotometer (Varian Cary 50 Scan, Agilent Technologies®, Santa Clara, CA, USA). The recirculating volume was approximately 50 mL and was continuously returned to the reactor, resulting in negligible variation in the total working volume and preserving hydrodynamic stability.

Each experimental run lasted 3 h and was divided into two sequential stages: an initial dark phase of 60 min followed by 120 min of UV irradiation. The dark period was introduced to establish adsorption–desorption equilibrium between Congo Red molecules and the photocatalyst surface, thereby decoupling purely adsorptive removal from true photocatalytic degradation, as commonly adopted in photocatalytic studies reported in the literature [43,44]. This step ensures that the subsequent decrease in concentration under irradiation can be attributed exclusively to photoinduced processes rather than to initial surface uptake phenomena.

UV–Vis spectra were acquired in the 400–800 nm range at 15 min intervals throughout the experiment. Spectral acquisition parameters were set to a scan rate of 1200 nm min^{-1}, wavelength resolution of 1 nm, and integration time of 0.05 s. Raw spectral data were processed according to the procedure detailed in Appendix A. This configuration ensured reproducible, quasi real-time tracking of concentration profiles under controlled irradiation and hydrodynamic conditions.

The complete experimental matrix, summarizing the irradiation conditions and associated operational parameters for each photocatalytic run, is reported in Table 1.

Table 1. Experimental conditions used for the photocatalytic degradation tests of Congo Red.

Light Intensity (mW cm^{-2})	Initial CR Concentration (ppm)	Catalyst Loading (ppm)	Dark Time (min)	Irradiation Time (min)
0.00	27.5	150	180	0
0.72	27.5	150	60	120
0.89	27.5	150	60	120
0.99	27.5	150	60	120

UV-VIS Calibration Curve

For quantitative analysis, Congo Red standard solutions were prepared in the concentration range 5–40 ppm (5, 10, 15, 20, 25, 30, 35, 40 ppm) by diluting a 500 ppm stock solution with distilled water. The selected interval brackets the expected experimental concentrations and ensures linear response of the analytical signal.

To account for matrix effects, standards were prepared in the presence of the same catalyst loading used during photocatalytic experiments. UV–Vis spectra were acquired under identical instrumental conditions and processed according to the multistep preprocessing procedure detailed in Appendix A. The analytical signal was defined as the maximum absorbance at 498 nm [45], determined from the full spectrum after blank correction. The calibration curve was constructed by plotting absorbance (A) versus concentration (C) and fitting the data by linear regression according to:

$$A = m\,C + q \tag{3}$$

where m represents the angular coefficient and q the intercept. The goodness of fit was evaluated through the coefficient of determination (R^2), and only models with $R^2 \geq 0.9999$ were accepted for quantitative analysis. All measurements were performed in duplicate,

https://doi.org/10.3390/su18094607

and the reported regression equation corresponds to averaged values. The resulting linear model was subsequently used to convert absorbance values of unknown samples into concentration values.

2.5. Mathematical Model

To quantitatively describe the temporal evolution of Congo Red concentration during the photocatalytic experiments, a simplified kinetic model was developed based on transient mass balance equations for a well-mixed batch system. The modeling framework builds upon our previously established formulation [46], which is here adapted to the present experimental configuration and briefly revisited to highlight the underlying assumptions and modifications introduced for the current setup.

Given the continuous magnetic stirring and the relatively small recirculating volume compared to the total working volume, the reactor was assumed to behave as an ideally mixed batch system with uniform concentration in the liquid phase. Under these conditions, spatial concentration gradients were neglected, and the system dynamics were described solely as a function of time.

From a mechanistic standpoint, the overall removal process involves two elementary phenomena: reversible adsorption of the dye onto the catalyst surface and irreversible photocatalytic degradation occurring from the adsorbed state under irradiation.

Direct homogeneous photolysis in the bulk liquid under UV irradiation was neglected. This assumption is supported by experimentally observed limited degradation of Congo Red in the absence of catalyst, as shown in Figure A1 (Appendix B), indicating that its contribution is negligible under the investigated conditions [47,48]. Furthermore, most photocatalytic kinetic models conventionally neglect direct photolysis, attributing dye removal predominantly to adsorption and catalyst-driven photoinduced reactions [49].

Additionally, mass transfer resistances were assumed to be negligible compared to the intrinsic kinetic steps.

Under these assumptions, the process can be represented by a lumped kinetic scheme involving two dynamic states: the dissolved dye concentration in the bulk liquid and the dye adsorbed on the catalyst surface [50,51]. This leads to the following kinetic scheme:

$$Dye \underset{k_2}{\overset{k_1}{\rightleftarrows}} Dye_A \overset{k_3}{\rightarrow} P \tag{4}$$

where Dye denotes the dissolved Congo Red molecules in the bulk liquid phase, Dye_A represents the dye adsorbed onto the photocatalyst surface, and P indicates the lumped degradation products formed through photocatalytic oxidation. The term P collectively includes intermediate species and final mineralization products (e.g., low-molecular-weight organic acids, CO_2, and H_2O), which are not individually resolved in the present model. The kinetic constants k_1 and k_2 account for adsorption/desorption, whereas k_3 represents the photoactivated degradation step and is switched on only upon irradiation. Under the above assumptions, the transient mass balance equations for the system can be expressed as:

$$\begin{cases} \frac{d[Dye]}{dt} = -k_1[Dye] + k_2[Dye_A] \\ \frac{d[Dye_A]}{dt} = k_1[Dye] - (k_2 + k_3)[Dye_A] \end{cases} \tag{5}$$

Along with the corresponding initial conditions:

$$\begin{bmatrix} [Dye] & [Dye_A] \end{bmatrix}\Big|_{t=0} = \begin{bmatrix} [Dye]^0 & [Dye_A]^0 \end{bmatrix} \tag{6}$$

The ODEs in reported in Equation (5) can be solved analytically, as detailed in Appendix C, yielding the general solution presented in Equation (A14).

In the present experimental setup, the system operates in two distinct temporal regimes corresponding to the dark adsorption phase and the subsequent irradiation phase. Therefore, the solution must be applied piecewise, with different initial conditions in each interval.

During the dark stage ($0 \leq t \leq t_{ON}$), irradiation is absent and thus $k_3 = 0$. The initial conditions at $t = 0$ are:

$$\begin{bmatrix} [Dye] & [Dye_A] \end{bmatrix}\Big|_{t=0} = \begin{bmatrix} [Dye]^0 & 0 \end{bmatrix} \tag{7}$$

since no adsorption has yet occurred at the beginning of the experiment. In this regime, the system evolves solely under adsorption–desorption dynamics and converges toward the adsorption equilibrium. The solution reported in Equation (A14) can thus be rewritten as:

$$\begin{cases} [Dye] = \frac{1}{k_1+k_2}[Dye]^0\left(k_2 - k_1 e^{-(k_1+k_2)t}\right) \\ [Dye_A] = \frac{k_1}{k_1+k_2}[Dye]^0\left(1 - e^{-(k_1+k_2)t}\right) \end{cases} \tag{8}$$

At $t = t_{ON}$, 60 min in the present experiments, irradiation is switched on and $k_3 > 0$. The concentrations reached at the end of the dark phase become the new initial conditions for the illuminated regime:

$$\underline{x}\big|_{t=t_{ON}} = \begin{bmatrix} [Dye]\big|_{t=t_{ON}} & [Dye_A]\big|_{t=t_{ON}} \end{bmatrix} \tag{9}$$

From this point onward, the full kinetic scheme, including photocatalytic degradation, governs the system dynamic. Hence, Equation (A14) takes the form:

$$\begin{cases} [Dye] = \frac{\Sigma+\sqrt{\Delta}}{2k_1\sqrt{\Delta}}\left[\left(k_1[Dye]^{ON} - \frac{1}{2}\left(\Sigma - \sqrt{\Delta}\right)[Dye_A]^{ON}\right)e^{\lambda_1 t} - \left(k_1[Dye]^{ON} - \frac{1}{2}\left(\Sigma + \sqrt{\Delta}\right)[Dye_A]^{ON}\right)e^{\lambda_2 t}\right] \\ [Dye_A] = \frac{1}{\sqrt{\Delta}}\left[\left(k_1[Dye]^{ON} - \frac{1}{2}\left(\Sigma - \sqrt{\Delta}\right)[Dye_A]^{ON}\right)e^{\lambda_1 t} - \left(k_1[Dye]^{ON} - \frac{1}{2}\left(\Sigma + \sqrt{\Delta}\right)[Dye_A]^{ON}\right)e^{\lambda_2 t}\right] \end{cases} \tag{10}$$

where Δ and Σ are defined as follows:

$$\Delta = (k_1 + k_2 + k_3)^2 - 4k_1k_3 \tag{11}$$

$$\Sigma = -k_1 + k_2 + k_3 \tag{12}$$

and λ_i denote the eigenvalues of the ODE system:

$$\lambda_1 = \frac{1}{2}\left[-(\Sigma + 2k_1) + \sqrt{\Delta}\right] \tag{13}$$

$$\lambda_2 = \frac{1}{2}\left[-(\Sigma + 2k_1) - \sqrt{\Delta}\right] \tag{14}$$

Light Intensity Dependence

The light dependence of the photocatalytic degradation rate was introduced through the definition of the kinetic constant k_3 as a linear function of the incident photon flux [52]. Specifically, the model assumes:

$$k_3 = a\ I \tag{15}$$

where I is the irradiation intensity and a is a proportionality parameter.

During the dark stage ($0 \leq t \leq t_{ON}$), the light-dependent term was set to zero ($k_3 = 0$), while after irradiation onset ($t > t_{ON}$), the degradation pathway was activated according to the relation above. This piecewise definition allows the model to explicitly account for the transition between adsorption-controlled dynamics and light-driven degradation within a unified kinetic framework [53].

2.6. Sensitivity Analysis: Model Based Taguchi Method

A model-based Taguchi design of experiments (DoE) was implemented to quantify the relative influence of the kinetic parameters governing the reaction scheme (Equation (4)) on the photocatalytic removal at 180 min [54,55]. The analysis was conducted using the dark–light kinetic formulation previously described in Section 2.5.

Three structural parameters (k_1, k_2 and a) were selected as control factors and investigated at five levels corresponding to ±50% variation around their globally fitted reference values (−50%, −25%, 0, +25%, +50%). This range was selected to represent a physically meaningful variability of the material properties while ensuring that the system remains within the same catalytic regime, avoiding parameter combinations that would correspond to fundamentally different materials.

An $L25\ (5^3)$ orthogonal array was adopted, resulting in 25 model evaluations per irradiation condition and enabling independent estimation of main effects with a substantially reduced number of combinations compared to a full factorial design [56].

For each orthogonal combination, the removal at 180 min was directly obtained from the analytical time-dependent solution of the previously derived stepwise kinetic model. To ensure comparability across irradiation conditions, the initial bulk dye concentration was fixed and set equal to the mean of the experimentally measured initial concentrations of the three irradiated runs, while the activated intermediate $[Dye_A]^0$ was imposed as zero. No additional assumptions were introduced.

Robustness and structural sensitivity of the response were evaluated through the Taguchi "larger-is-better" signal-to-noise (S/N) ratio [57]:

$$S/N_{F,l} = -10\log_{10}\left(\frac{1}{N_{F,l}}\sum_{i\in\Omega_{F,l}} y_i^{-2}\right) \tag{16}$$

where F denotes the considered factor (k_1, k_2 and a), l represents its level, $\Omega_{F,l}$ the subset of $L25$ combinations for which factor F assumes level l, $N_{F,l}$ the number of combinations in that subset, and y_i the simulated removal associated with combination i. For each pair (F,l), the S/N ratio $S/N_{F,l}$ was evaluated using exclusively the responses y_i with i in $\Omega_{F,l}$, thereby quantifying the structural effect of that specific factor level within the orthogonal design.

To complement the Taguchi screening, two-dimensional removal maps were generated using the analytical solution, while keeping k_1, k_2, and a fixed at their fitted reference values. In all configurations, the initial bulk dye concentration was kept again constant and set equal to the mean of the experimentally measured initial concentrations.

In the first configuration, removal was evaluated as a function of time and light intensity over a continuous photon flux range, imposing $[Dye_A]^0 = 0$ and a fixed dark–light switching time t_{ON}.

In the second configuration, light intensity was fixed at 0.89 mW cm^{-2}, catalyst fouling was represented by assigning a non-zero initial value to the activated state $[Dye_A]^0$. The admissible range of $[Dye_A]^0$ was constrained by the intrinsic limits of the reversible activation step, ensuring physical consistency. A detailed derivation of these constraints is provided in Appendix D.

3. Results and Discussion

3.1. Structural and Morphological Characterization

The XRD patterns (Figure 4A) of the Ag/Zn-NPs exhibited distinct diffraction peaks at 2θ values of 38.1°, 44.3° and 64.5°, corresponding to the (111), (200) and (220) crystallographic planes of Ag, respectively (Card No. 87–0720). Additional peaks at 2θ values of

32.8° and 55.0° attributed to (111) and (220), respectively (Card No. 75–1532) also confirm the formation of the cubic Pn-3m Ag_2O phase. Moreover, reflections corresponding to the hexagonal wurtzite structure of ZnO were observed (Card No. 75–0576), indicating the co-existence of separate Ag, Ag_2O, and ZnO phases within the NC.

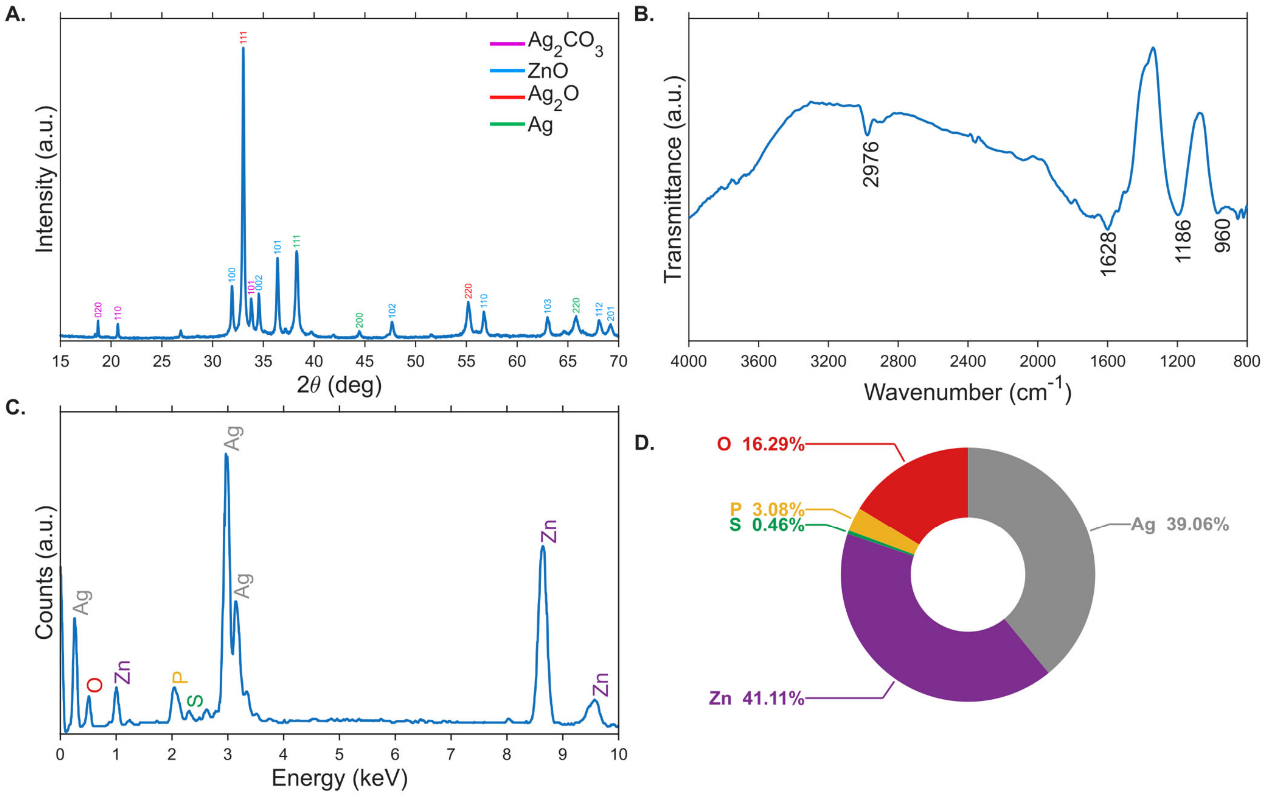

Figure 4. Structural and chemical characterization of the Ag/Zn-NPs nanocomposite. (**A**) XRD pattern showing the coexistence of ZnO wurtzite, metallic Ag, and Ag_2O phases. (**B**) FTIR spectrum indicating organic functional groups associated with the algal extract and $Zn-O$ vibrational bands. (**C**) EDX spectrum confirming the presence of Zn, O, and Ag elements. (**D**) Quantitative elemental composition obtained from EDX analysis.

The presence of Ag_2CO_3 (Card No. 70–2184) in the Ag/Zn-NPs is evidenced by characteristic XRD reflections. Such species could arise from residual bicarbonate ($NaHCO_3$) used as an inorganic carbon source during the cultivation of *Chlorella vulgaris*, which may be partially retained during biomass processing, as well as from carbonate-related functionalities associated with the organic constituents of the extract.

According to the Sherrer equation [58], the average crystallite sizes were estimated to be 32.76 nm for ZnO, 34.32 nm for Ag_2O, 24.28 nm for Ag, and 35.73 nm for Ag_2CO_3.

The functionalization by the extract was studied using FTIR analysis (Figure 4B). The spectra showed a peak near 2976 cm^{-1}, corresponding to $C-H$ stretching vibrations from aliphatic chains, indicating that polar lipid molecules might have a stabilizing role during the synthesis [59]. A band near 1628 cm^{-1} was observed, corresponding to the $C=O$ stretching vibration of amides, suggesting interactions between silver and proteinaceous components in the extract [59]. The peak at 1186 cm^{-1} can be attributed to $C=C$ stretching vibrations of aromatic rings and $C-O$ stretching vibrations [60], likely due to the adsorption of organic molecules from the extract used during synthesis. The peak at 960 cm^{-1} is indicative of $Zn-O$ stretching reported previously [61,62]. The results indicate the presence of both $Zn-O$ and organic capping agents on the Ag/Zn surfaces, suggesting a successful integration of Ag, Ag_2O, and ZnO components in the polar phase.

The SEM micrographs provide a coherent multiscale view of the material, revealing a hierarchically organized architecture extending from tens of micrometers down to the nanometric regime.

At low magnification (Figure 5A, 33.3 µm scale bar), the material appears as large, irregular macro-aggregates exceeding 30 µm in length. These aggregates are not compact monolithic structures, but rather loosely packed assemblies of smaller subunits. The surface is highly textured and heterogeneous, indicating that the macroscopic bodies originate from the coalescence of multiple secondary domains rather than from single crystal growth. This confirms that the material is structurally organized through aggregation processes rather than isolated particle formation.

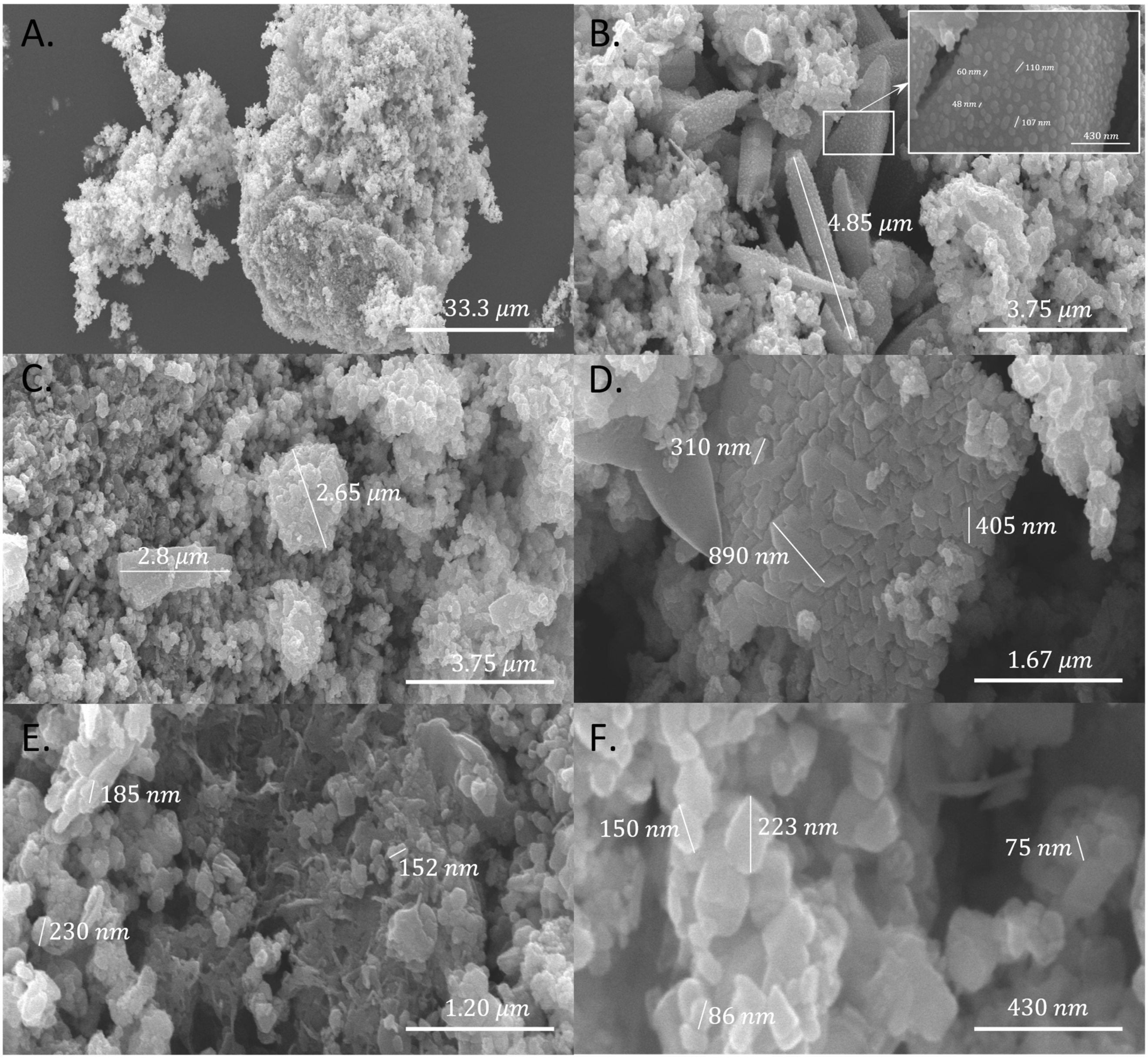

Figure 5. SEM micrographs of Ag/Zn-NPs nanocomposites at different magnifications showing the hierarchical morphology of the material. (**A**) Low-magnification image revealing large macro-aggregates. (**B**,**C**) Micrometric secondary domains composed of densely packed nanostructures. (**D**) Lamellar or flake-like domains embedded within the granular matrix. (**E**) Localized cavity-like region suggesting matrix-assisted assembly. (**F**) High-magnification image resolving the nanometric primary particles forming the hierarchical structure.

Increasing magnification (Figure 5B,C, 3.75 µm scale bar) reveals the internal organization of these macro-aggregates. The structure is composed of recurrent micrometric domains, typically in the 2.6–4.8 µm range, densely packed and interconnected. In Figure 5B, anisotropic elongated domains ($\sim$ 4.85 µm) are observed, exhibiting more defined boundaries compared to the surrounding granular matrix. Their rod- or platelet-like geometry suggests preferential growth along specific directions. The inset (430 nm scale bar) further shows that the surfaces of these micrometric domains are decorated with densely distributed and closely packed nanoscale nodular units (48–110 nm). This observation indicates that the micrometric domains themselves are secondary aggregates constructed from smaller nanometric building blocks.

Figure 5C emphasizes the recurrence and compact packing of these micrometric secondary aggregates. The structure appears highly interconnected, with minimal interstitial voids, reinforcing the interpretation of a hierarchical assembly where nanoscale primary units aggregate into micrometric clusters, which in turn assemble into larger macro-agglomerates.

At higher magnification (Figure 5D, 1.67 µm scale bar), a distinct morphological motif becomes evident: a lamellar or flake-like domain with lateral dimensions ranging from $\sim$ 310 to 890 nm. The surface exhibits a layered or terrace-like texture, with visible step edges and overlapping plates. This lamellar morphology contrasts with the predominantly granular texture observed in Panels B and C, suggesting that multiple growth pathways may coexist within the same material. Smaller granular particles appear attached to the flake surface, indicating that the lamellar domains are embedded within the broader nanoparticulate matrix.

A particularly noteworthy feature emerges in Figure 5E (1.20 µm scale bar). In contrast to the clearly particulate texture observed in other panels, the central region in this micrograph appears smoother, more continuous, and partially cavity-like. Rather than a purely granular assembly, this area exhibits a film-like or matrix-like morphology, suggestive of localized densification or collapse. Such a morphology may be consistent with the presence of a transient organic-derived phase during synthesis, potentially acting as a structuring or binding medium. Although direct confirmation would require complementary spectroscopic or thermal analyses, the observed "cavernous" or hollow-like region indicates that localized matrix-assisted assembly or shrinkage phenomena may have influenced particle organization in this area. This feature differentiates Panel E from the predominantly granular architecture seen elsewhere.

Finally, at the highest magnification (Figure 5F, 430 nm scale bar), the fundamental building units are clearly resolved. The particles are predominantly nanometric (75–220 nm), irregular, and often plate-like rather than spherical. Their angular geometry and visible particle–particle necking suggest strong interparticle contact and partial coalescence. The absence of large voids at this scale indicates a densely packed nanostructured framework.

Overall, the SEM analysis reveals a hierarchical architecture in which nanometric primary particles ($\approx$ 75–220 nm) assemble into micrometric secondary aggregates ($\approx$ 2.5–5 µm), which further coalesce into large macro-agglomerates ($>$ 20 µm). In addition to this dominant granular hierarchy, localized lamellar domains and cavity-like regions indicate the coexistence of anisotropic growth and possible matrix-mediated assembly mechanisms. This structural complexity suggests that the material formation process involves both particle aggregation and directional growth phenomena, leading to a multiscale, heterogeneous morphology.

The EDX spectra (Figure 4C) of the Ag/Zn-NPs synthesized from the polar extract showed prominent peaks corresponding to Ag and Zn, along with O likely associated with the ZnO and Ag_2O phases with P and S from the used extract. The corresponding quantitative analysis (Figure 4D) further confirms the dominance of Ag and Zn, supporting the successful formation of the intended composite structure. Notably, the silver content (39.06 wt%) is significantly higher than the values typically reported in the literature for Ag/ZnO systems (typically up to 5%) [63–67]. This indicates that silver is not present merely as a surface modifier but rather contributes to the formation of a multiphase system, potentially influencing both charge transfer dynamics and surface interactions. In this context, the photocatalytic behavior should be interpreted considering the combined effects of phase composition and interfacial processes, rather than solely in terms of conventional low loading Ag/ZnO configurations.

Mechanistic Insights into Bio-Mediated Synthesis and Phase Formation

The role of the *Chlorella vulgaris* polar extract can be interpreted in terms of coordination and stabilization rather than as a purely reductive agent. This aspect was previously discussed in detail in our earlier work [33], and is here briefly recalled for completeness. These interactions are facilitated by functional groups such as carboxyl, hydroxyl, and amino groups, which enable the formation of transient metal–ligand complexes [68].

Such coordination environments influence nucleation and growth processes. In the polar phase, the aqueous environment promotes efficient ion dissolution and facilitates interactions between metal ions and biomolecules, leading to the formation of nanoparticles that are potentially smaller and more uniform due to the stabilizing effects of hydrophilic capping agents. This behavior contrasts with the apolar phase, where stabilization is more restricted and primarily governed by lipid-mediated interactions. The ability of the polar phase to support efficient metal ion dissolution and complexation with biomolecules is therefore a key factor in controlling nanoparticle formation. Consistent with this interpretation, extracts of varying polarity have previously been employed for the synthesis of silver nanoparticles for catalytic and antimicrobial applications, demonstrating their influence on particle morphology and size [69–71].

Upon pH increase, the formation of metal hydroxides is induced. In the case of zinc, $Zn(OH)_2$ is formed and subsequently converted into ZnO during the calcination step [72]. For silver, the alkaline conditions promote the formation of silver and silver oxide species, which remain associated with the biomolecular matrix and with the ZnO surface during the second synthesis stage. The introduction of pre-formed ZnO nanoparticles provide a heterogeneous interface that facilitates the deposition and stabilization of silver-based species, leading to the formation of a multiphase composite [73]. In this framework, biomolecules from the extract act primarily as structure-directing and stabilizing agents, controlling particle dispersion and preventing excessive aggregation.

3.2. Optical Properties

The Tauc plot (Figure 6A) assuming a direct allowed transition revealed a band gap energy (E_g) of 3.240 eV, consistent with values reported for ZnO-based systems [74]. This value is slightly lower than that typically reported for bulk ZnO wurtzite (3.37 eV) [75], indicating a modest band-edge perturbation [76]. Such a red shift is commonly associated with structural disorder, defect formation, and interfacial electronic interactions in nanostructured or composite systems [77].

The Tauc plot displays two distinct linear regions: the high-energy segment corresponds to the intrinsic valence-to-conduction band transition, whereas the lower-energy segment is attributed to defect-induced sub-bandgap states, which modify the absorption edge and reflect a non-ideal band structure [78].

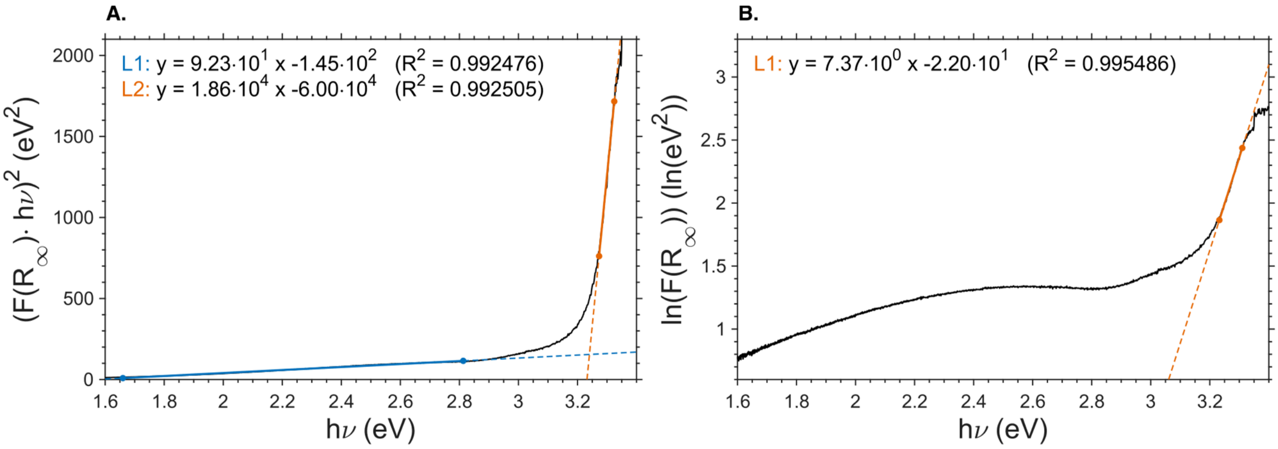

Figure 6. Optical characterization of the Ag/Zn-NPs nanocomposite obtained from diffuse reflectance spectroscopy. (**A**) Tauc plot assuming a direct allowed transition used to estimate the optical band gap energy: experimental data (black line), linear fits (blue and orange lines). (**B**) Urbach plot used to determine the Urbach energy and evaluate the degree of electronic disorder: experimental data (black line) and linear fit (orange line).

Further insight into the electronic disorder was obtained from the Urbach plot (Figure 6B), yielding an Urbach energy (E_U) of 0.136 eV. The relatively low Urbach energy, compared to literature values for similar systems (around 0.40 eV) [79,80], indicates a reduced density of band-tail states, suggesting a comparatively more ordered electronic structure with a sharper absorption edge [81].

While lower Urbach energy is generally associated with reduced electronic disorder, its direct correlation with photocatalytic activity is not straightforward. The presence and role of defect states in photocatalysis can be complex, as they may either act as recombination centers or contribute to charge separation depending on their nature and distribution. In this context, the relatively low Urbach energy suggests that defect-mediated states are not dominant, which may be beneficial for charge-carrier dynamics, although no direct causal relationship is implied.

3.3. Photodegradation Results

3.3.1. Calibration Line

Figure 7A shows the UV–Vis absorption spectra of the dye solutions in the 5–40 ppm concentration range. A single absorption band centered at 498 nm is observed. The absorbance increases proportionally with concentration while no shift in the peak position is detected, confirming compliance with the Beer–Lambert law. The calibration curve obtained from the absorbance at $\lambda = 498$ nm (Figure 7B) follows the linear regression:

$$A|_{\lambda=498\ nm} = 0.04434\ C + 0.1047 \tag{17}$$

with $R^2 = 0.999970$.

The high determination coefficient confirms the strong linear relationship between absorbance and concentration within the investigated range.

3.3.2. Photodegradation

Figure 8A–C illustrates the temporal evolution of dye concentration and removal efficiency under three irradiation intensities (0.72, 0.89 and 0.99 mW cm^{-2}). Two distinct regimes are clearly observed.

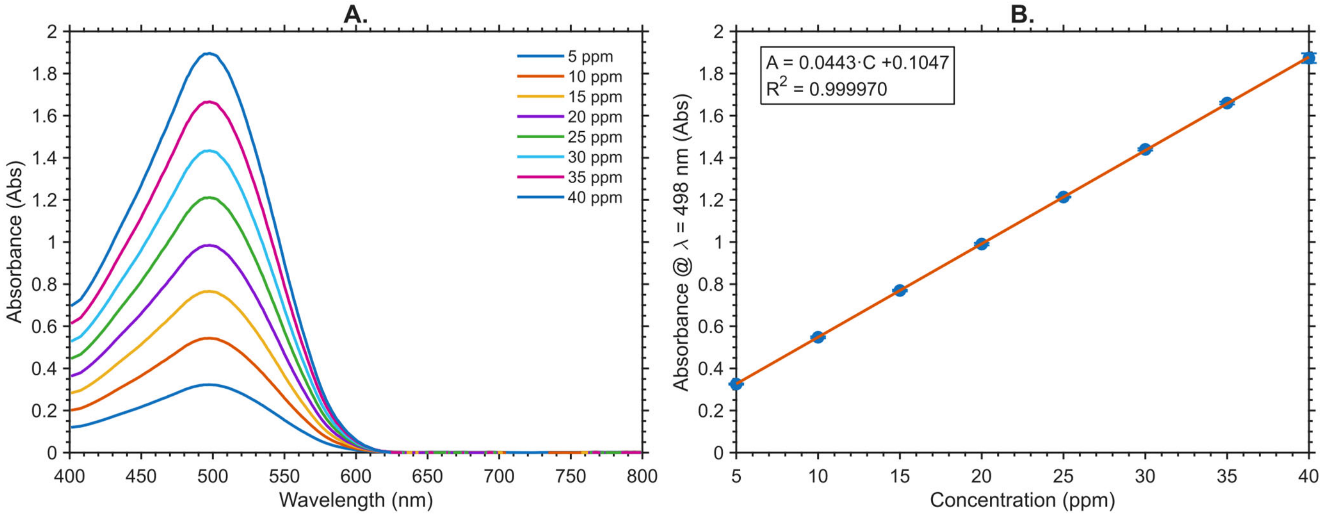

Figure 7. Calibration of Congo Red concentration by UV–Vis spectroscopy. (**A**) Absorption spectra of standard solutions in the investigated concentration range. (**B**) Calibration curve obtained from the absorbance at 498 nm showing the linear relationship between absorbance and dye concentration.

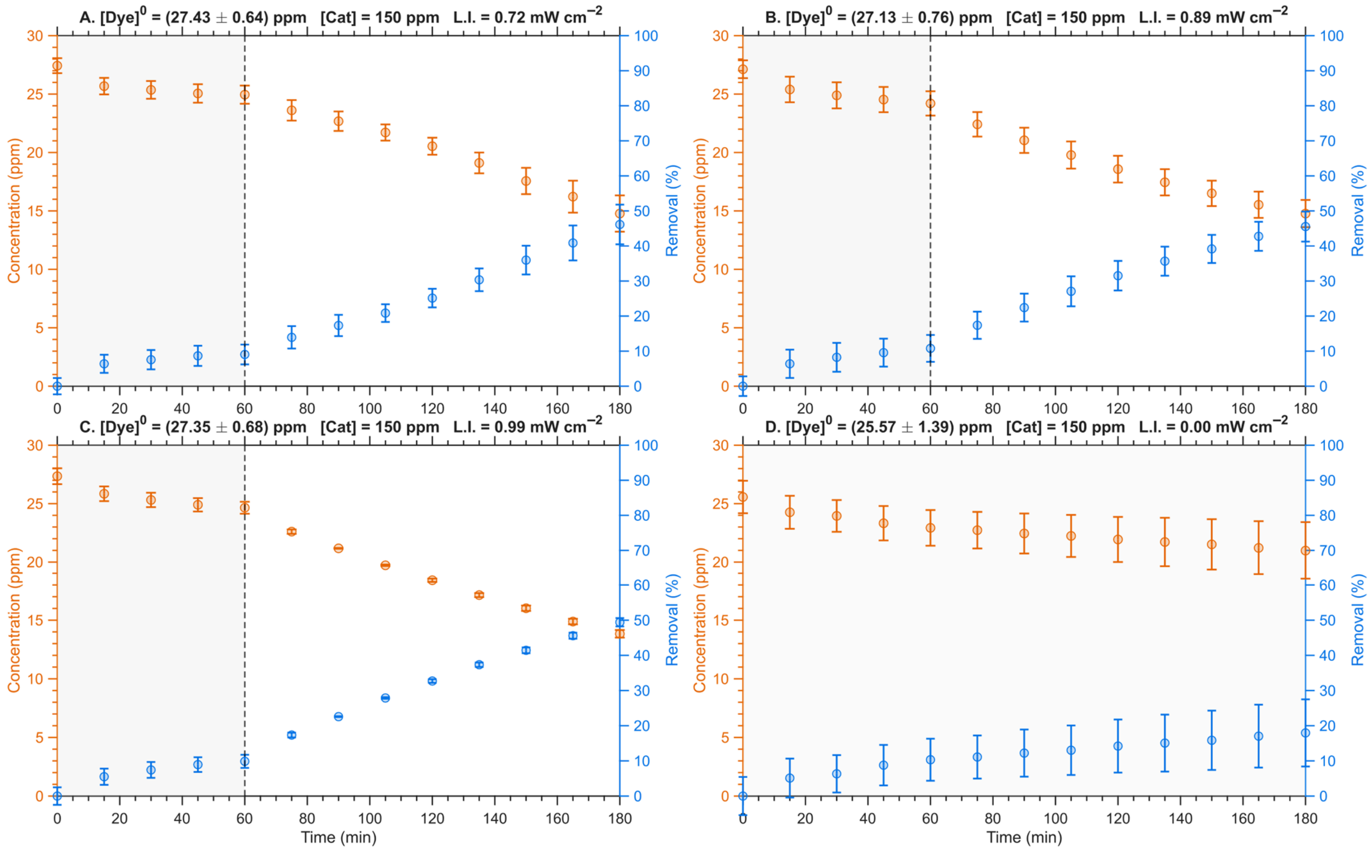

Figure 8. Temporal evolution of Congo Red concentration (orange symbols) and removal efficiency (blue symbols) during photocatalytic experiments under different irradiation conditions. Panels (**A**–**C**) correspond to UV irradiation intensities of 0.72, 0.89, and 0.99 mW cm^{-2}, respectively, while panel (**D**) represents the dark control experiment (0.00 mW cm^{-2}). The vertical dashed line indicates the transition between the dark adsorption stage (0–60 min) and the irradiation stage (60–180 min). Error bars represent the standard error of the mean (ε). The number of replicates is $n = 3$ for irradiated experiments and $n = 2$ for the dark control.

During the initial dark phase (0–60 min), all experiments exhibit a modest and comparable decrease in dye concentration. The overlapping trends across the three panels confirm that this stage is governed by adsorption–desorption equilibrium between dye molecules and the catalyst surface and is therefore independent of photon flux.

Upon light activation ($t = 60$ min), the system response changes markedly. A clear increase in the degradation rate is observed in all irradiated conditions, as evidenced by the steeper concentration decay and the progressive rise in removal efficiency. The smooth yet distinct transition between the dark and light regimes suggests that photogenerated reactive species act on pre-adsorbed dye molecules, indicating a surface-mediated photocatalytic mechanism rather than a purely homogeneous photolytic process.

The independent dark-control experiment (Figure 8D) provides a direct reference for this transition. In the absence of irradiation, the concentration approaches a quasi-steady adsorption-controlled regime and does not exhibit the accelerated decay observed in Figure 8A–C after light exposure. The clear divergence between the dark control and the irradiated profiles beyond 60 min confirms that the enhanced degradation rate originates from a light-driven pathway.

Quantitative comparison further supports this interpretation. At 60 min, all conditions, including the dark run, exhibit similar removal efficiencies, ranging between 9% and 11%, with no statistically meaningful differences within the standard error of the mean (ε), defined as the standard deviation divided by the square root of the number of replicates. This confirms that the initial stage is dominated by adsorption-controlled dynamics and remains independent of photon flux.

At 180 min, however, a clear separation emerges. The dark control reaches only $17.95 \pm 10.53\%$ removal, indicating limited additional adsorption-driven decay. In contrast, the irradiated systems achieve substantially higher efficiencies: $46.14 \pm 5.80\%$ at 0.72 mW cm^{-2}, $45.54 \pm 4.56\%$ at 0.89 mW cm^{-2}, and $49.41 \pm 1.73\%$ at 0.99 mW cm^{-2}. Despite the different photon fluxes, the three irradiated conditions remain statistically comparable within ε, indicating that, within the investigated intensity window, increasing light intensity does not result in a proportional enhancement of overall degradation performance.

This trend is visually summarized in Figure 9, where the grouped bar chart highlights the clear divergence between the dark- and light-driven systems at 180 min. While removal remains similar at 60 min across all conditions, a distinct separation appears at 180 min, with all irradiated runs clustering in the $\sim$ 45–50% range and the dark control remaining significantly lower.

The absence of a strong intensity dependence does not imply lack of photocatalytic activity. Rather, it suggests that once the light-induced pathway is activated, the system operates in a regime where the overall rate is not limited by photon availability. Secondary factors such as surface site saturation, adsorption equilibrium constraints, mass-transfer limitations, or charge recombination likely govern the global kinetics.

From an application standpoint, this behavior is particularly relevant: the catalyst achieves removal efficiencies approaching 50% even at the lowest tested intensity (0.72 mW cm^{-2}), and increasing photon flux up to 0.99 mW cm^{-2} does not yield statistically significant improvement. This indicates that the material operates near its effective photocatalytic regime under moderate irradiation conditions, highlighting its robustness and potential energy efficiency.

When positioned within the broader literature on Ag- and ZnO-based systems under UV irradiation, the present results fall within a clearly defined operational window. Over comparable reaction times of 60 to 180 min, degradation efficiencies ranging from about 80% to complete removal are frequently reported, generally in association with substantially higher catalyst loadings. For example, microwave assisted hydrothermal ZnO modified via borohydride reduction for silver deposition [82] achieved 81.6% degradation after 30 min of dark equilibration followed by 1 h of UV irradiation using 500 ppm catalyst at 16 ppm

Congo red. Hierarchical *ZnO* microstructures [83] reached 83.2% degradation for *ZnO* and 96.3% for the composite after 80 min of UV irradiation preceded by 30 min of dark equilibration, employing 800 ppm catalyst at 40 ppm Congo red.

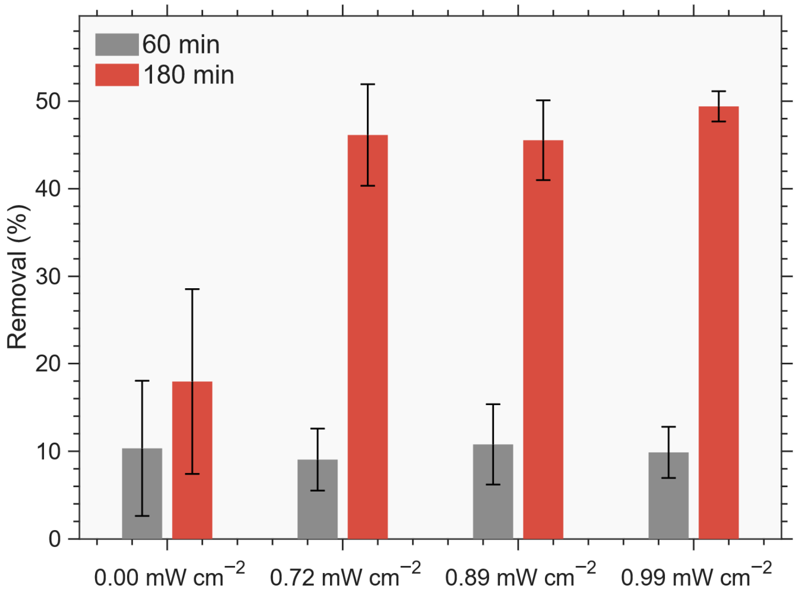

Figure 9. Comparison of Congo Red removal efficiencies at 60 min and 180 min under different irradiation intensities. The gray bars represent removal during the dark adsorption stage (60 min), while the red bars correspond to the final removal after 180 min. Error bars indicate the standard error of the mean (ε).

Similarly, *ZnO* hollow spheres and *Ag@ZnO* yolk–shell architectures [84] were evaluated after 1 h of dark adsorption–desorption equilibration, followed by UV irradiation using a catalyst loading of 500 ppm and an initial Congo Red concentration of 20 ppm. In that study, the *ZnO* hollow spheres required approximately 160 min of irradiation to achieve complete degradation, whereas the *Ag@ZnO* yolk–shell architecture reduced the required irradiation time to about 120 min under the same catalyst loading.

Recent studies on green-synthesized materials incorporating additional dopants, such as $Cu/Ag/ZnO$ systems obtained via *Vitex negundo* extracts [85], report Congo red degradation efficiencies up to $\sim$ 88% under UV irradiation within short reaction times (25 min, for an initial Congo red concentration of 50 ppm). However, these results are typically achieved at significantly higher catalyst loadings (1000 ppm) and do not exhibit a substantial step-change improvement compared to conventional Ag/ZnO systems.

Many high efficiency *Ag* and *ZnO* systems reported in the literature rely on multistep preparation routes, for example involving template assisted structuring or hydrothermal treatments [86,87]. These strategies, while effective in enhancing charge separation and surface area, increase material input, synthetic complexity, and thermal energy demand.

A similar trend is observed when moving to solar-driven systems. In a ZnO/Ag nanocomposite synthesized using lemon peel extract [88], Congo red degradation was evaluated at an initial concentration of 30 ppm using a catalyst loading of 1000 ppm. Under these conditions, pristine *ZnO* achieved about 77% degradation after 120 min, while ZnO/Ag reached approximately 86%, indicating a moderate improvement despite the high catalyst dosage.

A consistent behavior is also found in other green-synthesized Ag/ZnO systems tested under solar-simulated irradiation. Nanocomposites derived from *Ulva lactuca* extract achieved Congo red removal efficiencies exceeding 90% after 180 min under artificial sunlight, at an initial dye concentration of 30 ppm and a catalyst loading of 500 ppm [89].

Taken together, these observations suggest that high photocatalytic efficiencies, particularly under solar irradiation, are often obtained through a combination of elevated catalyst loadings and favorable irradiation conditions, rather than solely reflecting intrinsic material improvements. In this context, the comparison should not be based on the irradiation source alone. While some studies report higher Congo red removal under solar or solar simulated light, these results are often obtained using substantially larger catalyst dosages. By contrast, the present system was operated under UV irradiation with a comparatively low catalyst loading, highlighting a more restrained and materially efficient regime.

In this framework, the present study achieves approximately 45–50% degradation after 120 min of irradiation preceded by 60 min of dark equilibration, using a substantially lower catalyst loading (150 ppm). Although the absolute degradation efficiency is more moderate, it must be interpreted in relation to both catalyst dosage and irradiation conditions. When normalized to catalyst mass and accounting for the simplicity of the synthesis route, the performance of the present system falls within a competitive operational regime. From a process intensification and sustainability perspective, the combination of reduced catalyst dosage, moderate irradiation requirements, and simplified synthesis represents a meaningful step toward scalable and energetically rational photocatalytic water treatment.

3.4. Mathematical Model's Results

3.4.1. Parameters Estimation and Validation

Figure 10A–C compares the experimental dye concentration profiles with the trajectories reconstructed by the proposed kinetic model. The kinetic constants k_1, k_2 and the proportionality parameter a were estimated via nonlinear regression using the three irradiated experiments collected at low (0.72 mW cm^{-2}), medium (0.89 mW cm^{-2}), and high (0.99 mW cm^{-2}) photon flux (panels A–C). The fit was performed on the complete concentration–time series for each intensity, encompassing both the dark adsorption interval (0–60 min) and the irradiation interval (60–180 min), yielding an overall normalized root mean square error (NRMSE) of 3.14%. The optimized parameters are reported in Table 2. Specifically, the kinetic parameters, k_1, k_2 and a, were identified using the local optimization tool lsqcurvefit in Matlab® (The MathWorks Inc., version R2025a, Natick, MA, USA).

Table 2. Kinetic parameters obtained from nonlinear regression of the proposed dark–light kinetic model using the three irradiated experiments. Confidence intervals were calculated at the 95% level.

Parameter	Estimated Value	95% Confidence Interval	Unit
k_1	$8.53 \cdot 10^{-3}$	$[7.23 \quad 9.83] \cdot 10^{-3}$	min^{-1}
k_2	$7.64 \cdot 10^{-2}$	$[6.26 \quad 9.02] \cdot 10^{-2}$	min^{-1}
a	$1.12 \cdot 10^{-1}$	$[0.94 \quad 1.31] \cdot 10^{-1}$	cm^2 mW^{-1} min^{-1}

As shown in Figure 10A–C, a single parameter set consistently reproduces the experimental profiles under all photon flux conditions, with close agreement between measured data and simulated trajectories. During the dark phase (0–60 min), the model describes the gradual concentration decrease governed by adsorption–desorption dynamics. After irradiation onset ($t = 60$ min), the activation of the light-dependent pathway leads to a clear slope increase, which is accurately captured across all intensities.

To further assess the structural robustness of the kinetic formulation, the adsorption–desorption parameters k_1 and k_2, originally estimated from the three irradiated experiments (0–60 min dark stage followed by light exposure), were employed without any additional fitting to predict an independent dark-control experiment performed for the entire 0–180 min interval.

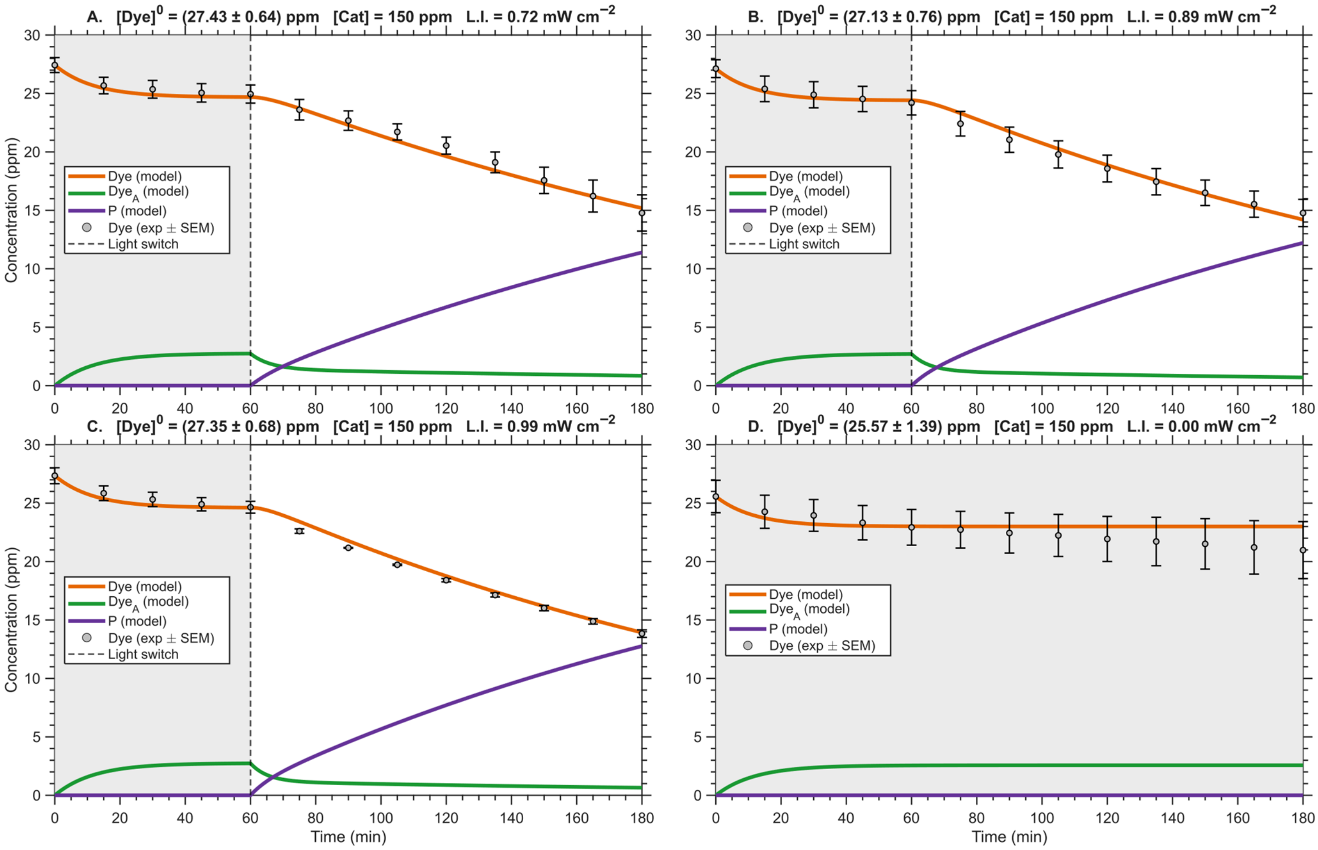

Figure 10. Comparison between experimental concentration profiles and model predictions obtained from the proposed kinetic formulation. (**A**–**C**) correspond to irradiated experiments at 0.72, 0.89, and 0.99 mW cm^{-2}, respectively. (**D**) shows the independent dark-control experiment. Symbols represent experimental measurements (mean ± ε), while solid lines denote the model predictions for dissolved dye (orange solid line), adsorbed intermediate (green solid line), and degradation products (violet solid line). The vertical dashed line marks the dark–light transition at 60 min.

In this validation test, the analytical solution was evaluated under the condition $k_3 = 0$ for the whole duration (Equation (8)), thus suppressing the photodegradation pathway. Importantly, although k_1 and k_2 were effectively informed only by the initial 60 min of dark data within the irradiated runs, the model accurately reproduces the concentration profile of the purely dark experiment up to 180 min (Figure 10D).

This predictive consistency demonstrates that the adsorption–desorption kinetics is correctly identified and that the additional concentration decay observed after irradiation onset in Figure 10A–C cannot be attributed to a slow continuation of dark dynamics.

Therefore, the agreement between the independently predicted dark control and the experimental measurements provides further mechanistic support for the proposed kinetic structure and reinforces the interpretation of the light-induced regime shift as genuine photocatalytic activity.

3.4.2. Sensitivity Analysis: Results

The main effects analysis of the signal-to-noise (S/N) ratio at 180 min (Figure 11) can be consistently interpreted considering the proposed kinetic scheme, where the dye reversibly forms an activated intermediate, which subsequently undergoes an irreversible light-dependent transformation to products. In this framework, the overall degradation performance is structurally controlled by the concentration and lifetime of the activated intermediate Dye_A, which acts as the reactive species driving product formation.

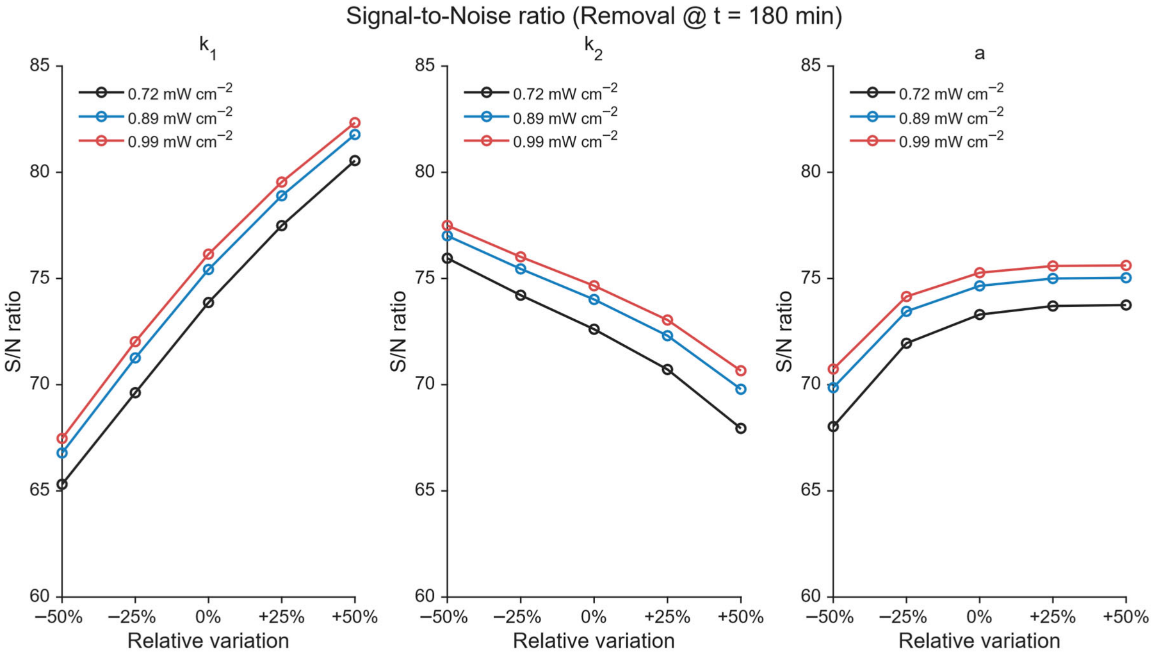

Figure 11. Main effects plots of the Taguchi signal-to-noise (S/N) ratio at 180 min showing the influence of the kinetic parameters k_1, k_2, and a on the degradation performance.

The parameter k_1, associated with the forward activation step exhibits a strong and monotonic positive effect on the S/N ratio across the entire investigated range. This behavior suggests that enhancing the rate of intermediate formation may contribute to improved dye removal efficiency. Mechanistically, a higher k_1 is expected to increase the fraction of Dye_A available for the irreversible transformation step, thereby potentially enhancing the productive reaction flux toward P. The absence of trend reversal in the main effects plot suggests that, within the explored domain, the system remains activation-limited rather than photon-limited. In other words, the ability to generate the reactive intermediate may represent a key structural constraint governing final conversion.

Conversely, k_2, which controls the reverse deactivation step, shows a pronounced negative effect on the S/N ratio. Increasing k_2 reduces the population of the activated intermediate by favoring its reconversion to the non-reactive form, thereby directly competing with the productive pathway. The clear monotonic decrease in S/N is indicative of the detrimental role in system performance. This highlights that the photocatalytic efficiency is not solely determined by light intensity or reaction irreversibility but critically depends on suppressing intermediate loss mechanisms.

In this context, the presence of algal-derived components plays a crucial mechanistic role. The algal matrix enhances dye adsorption, effectively capturing and retaining a larger fraction of dye molecules at the catalyst interface. This adsorption process increases the residence time of the dye in proximity to reactive sites [90], thereby favoring its conversion into the activated intermediate rather than allowing desorption or deactivation. As a result, the algal contribution can be interpreted as a structural factor that shifts the dynamic equilibrium toward productive pathways, improving overall degradation efficiency.

The parameter a, displays a different trend: the S/N ratio increases at low-to-moderate levels but tends to plateau at higher values [91]. This behavior appears to show that increasing light sensitivity initially enhances the conversion of the activated intermediate into products, leading to improved removal efficiency. However, beyond a certain threshold, further increases in a produce progressively smaller gains.

This may suggest that once the photoinduced step is sufficiently fast, the overall process is no longer limited by light-driven conversion but rather by the rate at which the activated intermediate is generated. In this regime, improving light responsiveness does not substantially increase performance because the bottleneck shifts upstream to intermediate formation. The observed plateau therefore reflects a transition from a light-assisted regime to one controlled by intrinsic activation kinetics.

Identifying this transition is particularly relevant from a practical standpoint, as further increases in irradiation intensity would not translate into proportional performance gains and may therefore lead to unnecessary energy consumption. In this context, the proposed kinetic framework can assist in identifying the onset of this regime and support more rational optimization of the operating conditions.

The nearly parallel trends observed for the three light intensities suggest weak interaction effects between intensity and the structural kinetic parameters. Light acts primarily as an additive scaling factor through Equation (15), shifting the absolute S/N level without altering the hierarchy or directionality of parameter influence. This reinforces the robustness of the kinetic model and confirms that the governing mechanism remains consistent across the irradiation conditions investigated.

Overall, the Taguchi analysis reveals that the photocatalytic system, within the investigated irradiation regime, is not purely photon-limited but fundamentally controlled by the dynamic equilibrium between activation and deactivation of the reactive intermediate. Efficient dye degradation requires maximizing the formation rate of Dye_A (high k_1), minimizing its loss through reverse pathways (low k_2), and ensuring sufficient photoinduced conversion. The coherence between statistical trends and mechanistic interpretation strongly supports the validity of the proposed kinetic scheme and provides a clear strategy for rational system optimization.

3.4.3. Effect of Light Intensity

In Figure 12A, dye removal is plotted as a function of time and light intensity, starting from an initial condition of $[Dye]^0 = 27.30$ ppm and $[Dye_A]^0 = 0$ ppm, with irradiation activated at 60 min. The horizontal dashed line clearly separates the dark adsorption regime from the irradiated regime. After irradiation begins, removal increases with both time and light intensity, but the color gradient reveals a strongly nonlinear behavior. At low intensities, removal grows gradually with time, whereas at moderate intensities a rapid transition toward high conversion is observed. However, beyond a certain light threshold, the improvement becomes progressively less pronounced, and the map tends toward a saturation region where further increases in intensity yield only marginal gains in final removal.

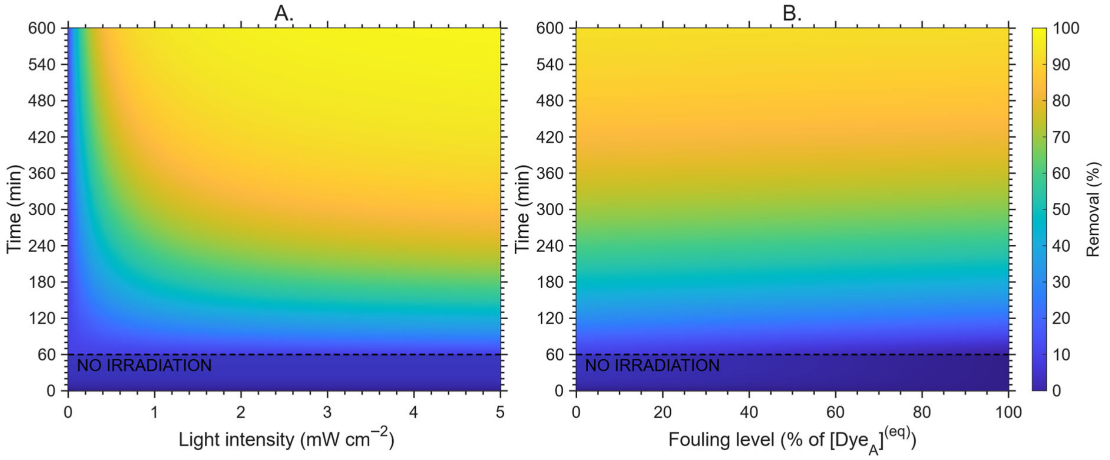

Figure 12. Model-based response surfaces obtained from the analytical kinetic solution. (**A**) Removal as a function of time and light intensity. (**B**) Removal as a function of time and initial surface fouling level at fixed irradiation intensity.

3.4.4. Effect of Fouling

Figure 12B explores a different but equally informative dimension: removal as a function of time and fouling level at a fixed intermediate light intensity. In contrast to Figure 12A, the color gradient is predominantly vertical, indicating that time is the dominant driver of removal under fixed irradiation. The relatively weak dependence on fouling level suggests that, within the explored range, the system maintains a stable kinetic response even as the initial dye burden increases. This behavior implies that the activated intermediate is not critically depleted under initially higher substrate loading and that the activation–deactivation equilibrium remains structurally balanced.

Notably, the absence of significant performance decay at increasing fouling levels provides indirect insight into catalyst robustness under pre-contaminated conditions. In this model, fouling is simulated as an increased initial amount of dye already adsorbed on the catalyst surface, representing a “pre-soiled” or partially covered catalyst prior to irradiation. The fact that degradation efficiency remains essentially unaffected by higher initial surface coverage suggests that the catalytic system does not suffer from severe site blocking or irreversible deactivation within the explored range.

The observed response indicates that the activated intermediate can still be efficiently formed and consumed even when a significant fraction of the surface is initially occupied. In other words, the dynamic balance between activation, deactivation, and photoinduced transformation appears capable of restoring active surface availability over time. Such resilience is highly relevant from an application standpoint, as it implies that surface coverage by organic species does not permanently suppress catalytic turnover.

Furthermore, the ability of the system to recover and maintain removal efficiency despite an initially “fouled” surface may suggest a self-regenerating or self-cleaning tendency under irradiation, where adsorbed dye molecules are progressively transformed into products rather than accumulated [92]. While dedicated cycling experiments would be required to confirm long-term stability and reusability, the model response indicates that the photocatalyst operates in a regime where transient surface coverage does not translate into persistent catalytic inhibition. This behavior is consistent with a dynamically regenerated active surface under continuous illumination.

4. Conclusions

This study demonstrates that the green-synthesized Ag/Zn-NPs derived from *Chlorella vulgaris* polar extract consist of a multiphase system combining wurtzite ZnO with metallic Ag and Ag_2O, as confirmed by XRD analysis. SEM observations revealed a hierarchical morphology, with nanometric primary particles assembled into micrometric aggregates, while FTIR analysis confirmed the presence of organic functional groups associated with the algal extract on the material surface. Diffuse reflectance analysis, based on the Tauc method, yielded a band gap energy of 3.24 eV, while the Urbach energy was found to be relatively low (0.135 eV), indicating a limited density of band-tail states.

Sequential dark–light experiments (60 min dark plus 120 min UV) clearly separated adsorption equilibrium ($\sim$ 9–11% removal) from photoactivated degradation, leading to final efficiencies of $\sim$ 44–49% at 180 min using 150 ppm catalyst and 27.5 ppm initial Congo Red.

The analytical kinetic model quantitatively reproduced all irradiation conditions and successfully predicted an independent 180 min dark-control experiment without additional fitting, confirming the structural validity of the adsorption–activation–degradation scheme. The weak dependence of removal efficiency on photon flux within the investigated range indicates operation beyond a strictly photon-limited regime, highlighting intrinsic energy robustness governed by intermediate dynamics rather than light intensity alone. This provides a mechanistic basis for interpreting the observed plateau in removal efficiency and highlights the relevance of intermediate-mediated pathways in determining system behavior. At the same time, the present analysis is inherently constrained to the investigated operating window, and extending the exploration to a broader range of irradiation conditions would be necessary to fully map the transition between photon-limited and kinetically controlled regimes. In this perspective, future work should focus on coupling the present analytical framework with extended experimental conditions to further generalize the identified behavior.

Importantly, competitive performance is achieved at relatively low catalyst loading through a bio-mediated synthesis route. By integrating renewable biomass valorization, reduced material input, and mechanistically validated kinetics, this work advances a systems-level sustainability framework that aligns green chemistry, energy-conscious operation, and circular resource utilization for water remediation applications. From a broader sustainability perspective, the results further suggest that efficient operation can be achieved without increasing photon input or catalyst loading, pointing toward a favorable balance between material use and energy demand. However, the present study does not explicitly address key metrics such as catalyst reusability, long-term stability, or process-level energy efficiency, which are essential for a comprehensive sustainability assessment. Future investigations should therefore integrate these aspects, including durability testing and energy-performance analysis, to fully evaluate the practical viability of the proposed system within real-world water treatment scenarios.

Overall, this work highlights how the integration of green synthesis, kinetic insight, and process-oriented thinking can guide the development of next-generation photocatalytic systems for sustainable water remediation.

Author Contributions: Conceptualization, F.Z., R.L. and A.C.; Methodology, F.Z., F.A., A.S., R.L. and A.C.; Software, F.Z. and F.A.; Validation, F.Z., F.A., S.C., A.S., G.F. and F.D.; Formal analysis, F.Z., F.A. and R.L.; Investigation, F.Z., S.C., A.S. and G.F.; Resources, G.F., F.D., S.P. and G.A.L.; Data curation, F.Z., S.C. and A.S.; Writing—original draft preparation, F.Z. and A.S.; Writing—review and editing, F.Z., F.A., S.C., A.S., G.F., F.D., R.L., S.P., G.C., G.A.L. and A.C.; Visualization, F.Z.; Supervision, R.L. and A.C. All authors have read and agreed to the published version of the manuscript.

Funding: This research received no external funding.

Data Availability Statement: The original contributions presented in this study are included in the article. Further inquiries can be directed to the corresponding authors.

Acknowledgments: F.Z., F.A. and S.C. performed their work within the framework of the International PhD in Innovation Sciences and Technologies at the University of Cagliari, Italy.

Conflicts of Interest: Giovanni Antonio Lutzu was employed by the Teregroup Srl. The remaining authors declare that the research was conducted in the absence of any commercial or financial relationships that could be construed as a potential conflict of interest.

Appendix A. Data Treatment

UV–Vis spectra were processed through a structured multistep workflow implemented in MATLAB® (The Mathworks Inc., version R2025a, Natick, MA, USA). As a first step, a linear baseline correction was applied to compensate for background contributions arising primarily from light scattering due to suspended photocatalyst particles (turbidity effects). In heterogeneous photocatalytic systems, the presence of solid particles induces wavelength-dependent scattering, particularly noticeable in the high-wavelength region where Congo Red absorption is negligible. Therefore, the spectral interval between 700 and 800 nm was fitted using a first-order polynomial, assuming minimal dye absorption in this range. The resulting linear baseline was subtracted from the entire spectrum to isolate the true absorbance contribution of the dissolved species.

Subsequently, noise reduction was carried out using a principal component analysis (PCA)-based reconstruction approach [93]. The spectral matrix was column-wise standardized (z-score normalization) prior to PCA application. The spectra were reconstructed by retaining the minimum number of principal components required to explain at least 90% of the cumulative variance, thereby preserving the chemically relevant information while suppressing high-frequency instrumental noise.

A final smoothing step was performed using a moving-average filter applied along the wavelength axis to further improve signal stability without altering spectral features.

Replicate experiments were processed following the identical workflow and combined to calculate mean values and the associated standard errors of the mean.

Appendix B. Control Experiment: Direct Photolysis of Congo Red

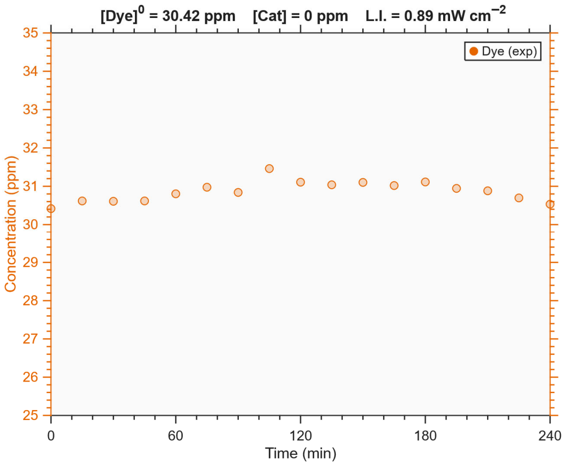

Figure A1. Control experiment under UV irradiation ($L.I. = 0.89$ mW cm^{-2}) in the absence of catalyst ($[Cat] = 0$ ppm) showing the temporal evolution of Congo Red concentration $\left([Dye]^0 = 30.42 \text{ ppm}\right)$. No significant variation in dye concentration is observed over 240 min.

Appendix C. Derivation of the Analytical Solution

In compact vector form, the system reported in Equation (5) can be rewritten as:

$$\underline{\dot{x}} = \underline{\underline{A}}\,\underline{x} \tag{A1}$$

subject to the following starting conditions:

$$\underline{x}\big|_{t=0} = \left[[Dye]^0 \quad [Dye_A]^0 \right] \tag{A2}$$

Owing to the linear structure of the system, the temporal evolution of the state vector can be expressed in terms of the eigenvalues and eigenvectors of the kinetic matrix $\underline{\underline{A}}$. The eigenvalues were obtained from the characteristic equation:

$$\det\left(\underline{\underline{A}} - \lambda \underline{\underline{I}} \right) = \begin{vmatrix} -(k_1+\lambda) & k_2 \\ -k_1 & -(k_2+k_3+\lambda) \end{vmatrix} = (k_1+\lambda)(k_2+k_3+\lambda) - k_1 k_2 = 0 \tag{A3}$$

which, upon solution, yields the following eigenvalues:

$$\lambda_{1,2} = \frac{1}{2}\left[-(k_1+k_2+k_3) \pm \sqrt{(k_1+k_2+k_3)^2 - 4k_1k_3} \right] \tag{A4}$$

The corresponding eigenvectors $\underline{v}_{\,i}$ were then determined by solving the homogeneous linear system associated with each eigenvalue λ_i:

$$\left(\,\underline{\underline{A}} - \lambda_i \underline{\underline{I}}\,\right)\underline{v}_{\,i} = \underline{0} \tag{A5}$$

expanding the system explicitly:

$$\begin{cases} -(k_1 + \lambda_i)v_{1,i} + k_2 v_{2,i} = 0 \\ k_1 v_{1,i} - (k_2 + k_3 + \lambda_i)v_{2,i} = 0 \end{cases} \tag{A6}$$

Since λ_i satisfies the characteristic equation, Equation (A3), the two equations of the homogeneous system are not independent. This can be demonstrated explicitly. In fact, from Equation (A3) the term k_2 can be expressed as a function of λ_i, k_1, k_2 itself and k_3. Substituting this relation into the first equation of the system reported in Equation (A6) and multiplying by $-k_1$, it follows, upon use of the characteristic equation, that the first equation reduces to the same algebraic condition of the second equation:

$$k_1 v_{1,i} - (k_2 + k_3 + \lambda_i)v_{2,i} = 0 \tag{A7}$$

Therefore, the two equations are linearly dependent, and the system admits only one independent constraint, allowing the eigenvector components to be determined up to an arbitrary multiplicative constant α:

$$\underline{v}_{\,i} = \alpha \begin{bmatrix} 1 & \frac{k_1}{k_2 + k_3 + \lambda_i} \end{bmatrix}^T \tag{A8}$$

without loss of generality, setting $\alpha = 1$, the matrix of eigenvectors can be written as:

$$\underline{\underline{V}} = \begin{bmatrix} \underline{v}_{\,1} & \underline{v}_{\,2} \end{bmatrix} = \begin{bmatrix} v_{1,1} & v_{1,2} \\ v_{2,1} & v_{2,2} \end{bmatrix} = \begin{bmatrix} 1 & 1 \\ \frac{k_1}{k_2 + k_3 + \lambda_1} & \frac{k_1}{k_2 + k_3 + \lambda_2} \end{bmatrix} \tag{A9}$$

Under these conditions, the general solution of linear system can be expressed as a linear combination of the eigenmodes:

$$\underline{x} = C_1 \underline{v}_{\,1} e^{\lambda_1 t} + C_2 \underline{v}_{\,2} e^{\lambda_2 t} \tag{A10}$$

where C_1 and C_2 are constants determined by the initial conditions reported in Equation (A2). Imposing the initial state $\underline{x}|_{t=0} = \underline{x}^0$, one obtains:

$$\underline{x}^0 = C_1 \underline{v}_{\,1} + C_2 \underline{v}_{\,2} \tag{A11}$$

which leads to a linear algebraic system for C_1 and C_2. Solving this system by inversion of the eigenvector matrix $\underline{\underline{V}}$, the coefficients are given by:

$$\begin{cases} C_1 = \frac{v_{2,2}[Dye]^0 - v_{1,2}[Dye_A]^0}{det\left(\,\underline{\underline{V}}\,\right)} \\ C_2 = -\frac{v_{2,1}[Dye]^0 - v_{1,1}[Dye_A]^0}{det\left(\,\underline{\underline{V}}\,\right)} \end{cases} \tag{A12}$$

Substituting the expressions of C_1 and C_2 into the general solution and rearranging terms, the state vector can be written explicitly as:

$$\underline{x} = \frac{v_{2,2}[Dye]^0 - v_{1,2}[Dye_A]^0}{det\left(\,\underline{\underline{V}}\,\right)}\,\underline{v}_{\,1} e^{\lambda_1 t} - \frac{v_{2,1}[Dye]^0 - v_{1,1}[Dye_A]^0}{det\left(\,\underline{\underline{V}}\,\right)}\,\underline{v}_{\,2} e^{\lambda_2 t} \tag{A13}$$

Extracting the individual components of the state vector yields the explicit time evolution of the dissolved and adsorbed dye concentrations:

$$\begin{cases} [Dye] = \frac{v_{2,2}[Dye]^0 - v_{1,2}[Dye_A]^0}{det(\underline{\underline{V}})} v_{1,1}\, e^{\lambda_1 t} - \frac{v_{2,1}[Dye]^0 - v_{1,1}[Dye_A]^0}{det(\underline{\underline{V}})} v_{1,2}\, e^{\lambda_2 t} \\ [Dye_A] = \frac{v_{2,2}[Dye]^0 - v_{1,2}[Dye_A]^0}{det(\underline{\underline{V}})} v_{2,1}\, e^{\lambda_1 t} - \frac{v_{2,1}[Dye]^0 - v_{1,1}[Dye_A]^0}{det(\underline{\underline{V}})} v_{2,2}\, e^{\lambda_2 t} \end{cases} \tag{A14}$$

Eigenvalues Properties

It is worth noting that both eigenvalues are real and non-positive. In the present experimental setup, a dark adsorption phase precedes irradiation, such that the kinetic constants k_1 and k_2 are determined independently before the photocatalytic step is activated. The light-induced rate constant k_3 is introduced only after the switching time t_{ON}, when irradiation is applied. For fixed values of k_1 and k_2 established during the dark regime, there exists no physically admissible value of k_3 that makes the discriminant of the characteristic polynomial negative. Consequently, the eigenvalues remain real under all meaningful operating conditions of the present system, and no oscillatory behavior can arise.

In the absence of irradiation ($k_3 = 0$), one eigenvalue is zero, corresponding to a marginally stable mode associated with the adsorption/desorption equilibrium established between the bulk liquid Dye and the surface-adsorbed species. The second eigenvalue remains strictly negative, ensuring convergence toward this equilibrium state.

When irradiation is applied ($k_3 > 0$), both eigenvalues become strictly negative. Under these conditions, the system is asymptotically stable, and the unique equilibrium point shifts to the origin, corresponding to complete depletion of both dissolved and adsorbed dye concentrations. The eigenvalues are given by Equation (A4), for the eigenvalues remain real, the discriminant must satisfy:

$$(k_1 + k_2 + k_3)^2 - 4k_1k_3 > 0 \tag{A15}$$

expanding the expression yields a quadratic function of k_3:

$${k_3}^2 + 2(k_2 - k_1)k_3 + (k_2 + k_1)^2 > 0 \tag{A16}$$

The corresponding equality leads to:

$${k_3}^{(1,2)} = \frac{1}{2}\left[-(k_2 - k_1) \pm \sqrt{-4k_1k_2}\right] \tag{A17}$$

Since $k_1 > 0$ and $k_2 > 0$ represent kinetic rate constants, the term under the square root becomes negative ($-4k_1k_2 < 0$), implying that the roots of Equation (A16) are complex conjugates. Consequently, the quadratic expression in Equation (A17) remains strictly positive for any real value of k_3, and for $k_3 > 0$. Therefore, when irradiation is present, both eigenvalues are always real and negative, confirming that the system is asymptotically stable and that the dynamical trajectories converge monotonically toward the zero-concentration equilibrium. This result reflects the irreversible photochemical sink introduced by the light-driven step, which removes activated dye molecules from the reversible adsorption–desorption cycle and drives the system toward complete depletion.

Appendix D. Fouling

By imposing $k_3 = 0$ in Equation (A14), corresponding to the absence of irradiation, the system reduces to the purely reversible adsorption–desorption dynamics. The analytical solution becomes

$$\begin{cases} [Dye] = \frac{k_2}{k_1+k_2}\left([Dye]^0 + [Dye_A]^0\right) + \frac{k_1[Dye]^0 - k_2[Dye_A]^0}{k_1+k_2} e^{-(k_1+k_2)t} \\ [Dye_A] = \frac{k_1}{k_1+k_2}\left([Dye]^0 + [Dye_A]^0\right) - \frac{k_1[Dye]^0 - k_2[Dye_A]^0}{k_1+k_2} e^{-(k_1+k_2)t} \end{cases} \tag{A18}$$

In the limit $t \to \infty$, the exponential term vanishes and the system approaches the adsorption–desorption equilibrium state

$$\begin{cases} [Dye]^{(eq)} = \frac{k_2}{k_1+k_2}\left([Dye]^0 + [Dye_A]^0\right) \\ [Dye_A]^{(eq)} = \frac{k_1}{k_1+k_2}\left([Dye]^0 + [Dye_A]^0\right) \end{cases} \tag{A19}$$

The equilibrium value $[Dye_A]^{(eq)}$ represents the maximum amount of dye that can be adsorbed on the catalyst surface under the given conditions. Consequently, the initial surface concentration must satisfy the physical constraint:

$$[Dye_A]^0 < \frac{k_1}{k_2}[Dye]^0 \tag{A20}$$

to ensure that the initially occupied surface fraction does not exceed the equilibrium adsorption capacity. This formulation allows the model to represent partial surface pre-occupation (e.g., catalyst fouling or incomplete regeneration) without altering the bulk mass conditions.

In the simulations, the initial adsorbed fraction was therefore parameterized as

$$[Dye_A]^0 = f\frac{k_1}{k_2}[Dye]^0 \tag{A21}$$

where $f \in [0,1]$ represents the fraction of the maximum equilibrium adsorption capacity initially occupied.

References

1. Abalasei, M.E.; Toma, D.; Dorus, M.; Teodosiu, C. The Impact of Climate Change on Water Quality: A Critical Analysis. *Water* **2025**, *17*, 3180. [CrossRef]
2. Simonetti, F.; Brillarelli, S.; Agostini, M.; Mancini, M.; Gioia, V.; Murtas, S.; Migliorati, V. A Review on the Latest Frontiers in Water Quality in the Era of Emerging Contaminants: A Focus on Perfluoroalkyl Compounds. *Environ. Pollut.* **2025**, *381*, 126402. [CrossRef]
3. Qiao, X.; Ning, S.; Zhao, H.; Ni, R.; Zhang, W.; Zhang, Y.; Zhai, L.; Shang, D.; Wang, Y.; Yang, T.; et al. Integrating Photo-Fenton-like Fe3O4/CdS-O Modules into Sponge-Based Gel Solar Evaporator for Synergistic Water Regeneration and Pollutant Degradation. *J. Environ. Chem. Eng.* **2025**, *13*, 117247. [CrossRef]
4. Ochs, C.; Garrison, K.; Saxena, P.; Romme, K.; Sarkar, A. Contamination of Aquatic Ecosystems by Persistent Organic Pollutants (POPs) Originating from Landfills in Canada and the United States: A Rapid Scoping Review. *Sci. Total Environ.* **2024**, *924*, 171490. [CrossRef]
5. Abhisek, K.; Vhatkar, S.S.; Mathew, H.T.; Singh, P.; Oraon, R. A Critical Review on the Challenges and Techno-Economic Assessment of Dyes Removal Technologies from Waste Water. *Discov. Chem.* **2025**, *2*, 41. [CrossRef]
6. Amar, I.A.; Nouh, A.A.; Aljarani, A.M.; Shamsi, S.S.; Ghosh, K.S.; Hosseini-Bandegharaei, A. Surfactant-Assisted Co-Precipitation Synthesis of Zn-Doped Tin Ferrite for Methylene Blue and Congo Red Dyes Photodegradation and Phytotoxicity Studies. *Chem. Afr.* **2025**, *8*, 5555–5588. [CrossRef]
7. Lade, H.; Govindwar, S.; Paul, D. Mineralization and Detoxification of the Carcinogenic Azo Dye Congo Red and Real Textile Effluent by a Polyurethane Foam Immobilized Microbial Consortium in an Upflow Column Bioreactor. *Int. J. Environ. Res. Public Health* **2015**, *12*, 6894–6918. [CrossRef]
8. Siddiqui, S.I.; Allehyani, E.S.; Al-Harbi, S.A.; Hasan, Z.; Abomuti, M.A.; Rajor, H.K.; Oh, S. Investigation of Congo Red Toxicity towards Different Living Organisms: A Review. *Processes* **2023**, *11*, 807. [CrossRef]
9. Bani-Atta, S.A.; Darwish, A.A.A.; Alatawi, N.M.; Alkhathami, N.D.; Al-Tweher, J.N.; El-Zaidia, E.F.M. Efficient Photodegradation of Congo Red and Phenol Red in Wastewater Using Nanosized Cu-Polyoxometalate: A Promising UV-Active Catalyst for Environmental Treatment. *Catalysts* **2025**, *15*, 920. [CrossRef]
10. Khan, M.I.; Akhtar, S.; Zafar, S.; Shaheen, A.; Khan, M.A.; Luque, R.; Ur Rehman, A. Removal of Congo Red from Aqueous Solution by Anion Exchange Membrane (EBTAC): Adsorption Kinetics and Themodynamics. *Materials* **2015**, *8*, 4147–4161. [CrossRef]

11. Khader, E.H.; Muslim, S.A.; Saady, N.M.C.; Ali, N.S.; Salih, I.K.; Mohammed, T.J.; Albayati, T.M.; Zendehboudi, S. Recent Advances in Photocatalytic Advanced Oxidation Processes for Organic Compound Degradation: A Review. *Desalination Water Treat.* **2024**, *318*, 100384. [CrossRef]
12. Zhu, H.; Wang, Z.; Cao, L.; Wang, Y.; Zhang, Y.; Shang, D.; Zhai, L.; Yang, T.; Yang, F. Constructing Electron-Deficient Co Centers in the Lattice of Oxygen-Vacancy-Rich CuO for Improved PMS Activation and Contaminant Degradation. *Chem. Commun.* **2025**, *61*, 7065–7068. [CrossRef]
13. Mohod, A.V.; Momotko, M.; Shah, N.S.; Marchel, M.; Imran, M.; Kong, L.; Boczkaj, G. Degradation of Rhodamine Dyes by Advanced Oxidation Processes (AOPs)—Focus on Cavitation and Photocatalysis—A Critical Review. *Water Resour. Ind.* **2023**, *30*, 10020. [CrossRef]
14. Xu, H.Y.; Zhang, S.Q.; Wang, Y.F.; Xu, Y.; Dong, L.M.; Komarneni, S. New Insights into the Photocatalytic Mechanism of Pristine ZnO Nanocrystals: From Experiments to DFT Calculations. *Appl. Surf. Sci.* **2023**, *614*, 156225. [CrossRef]
15. Zhao, H.-Y.; Wang, S.; Zhu, H.-Y.; Zhang, X.-X.; Shang, D.-H.; Zhou, X.-W.; Wang, J.; Zhu, C.-Z.; Du, F.; Song, Y.-Y.; et al. Modulating Nanograin Size and Oxygen Vacancy of Porous ZnO Nanosheets by Highly Concentrated Fe-Doping Effect for Durable Visible Photocatalytic Disinfection RARE METALS. *Rare Met.* **2024**, *43*, 5905–5920. [CrossRef]
16. Gao, S.; Yang, F.; Song, C.; Cai, Q.; Wang, R.; Zhou, S.; Kong, Y. Photocatalytic Producing Dihydroxybenzenes from Phenol Enabled by Gathering Oxygen Vacancies in Ultrathin Porous ZnO Nanosheets. *Appl. Surf. Sci.* **2020**, *505*, 144580. [CrossRef]
17. Dinesh, V.P.; Biji, P.; Ashok, A.; Dhara, S.K.; Kamruddin, M.; Tyagi, A.K.; Raj, B. Plasmon-Mediated, Highly Enhanced Photocatalytic Degradation of Industrial Textile Dyes Using Hybrid ZnO@Ag Core-Shell Nanorods. *RSC Adv.* **2014**, *4*, 58930–58940. [CrossRef]
18. Loka, C.; Lee, K.S. Enhanced Visible-Light-Driven Photocatalysis of Ag/Ag2O/ZnO Nanocomposite Heterostructures. *Nanomaterials* **2022**, *12*, 2528. [CrossRef]
19. Singh, S.; Perween, S.; Ranjan, A. Dramatic Enhancement in Adsorption of Congo Red Dye in Polymer-Nanoparticle Composite of Polyaniline-Zinc Titanate. *J. Environ. Chem. Eng.* **2021**, *9*, 105149. [CrossRef]
20. Khan, S.H. Green Nanotechnology for the Environment and Sustainable Development. In *Green Materials for Wastewater Treatment*; Naushad, M., Lichtfouse, E., Eds.; Springer International Publishing: Cham, Switzerland, 2020; pp. 13–46. ISBN 978-3-030-17724-9.
21. Cruz, D.M.; Mostafavi, E.; Vernet-Crua, A.; Barabadi, H.; Shah, V.; Cholula-Díaz, J.L.; Guisbiers, G.; Webster, T.J. Green Nanotechnology-Based Zinc Oxide (ZnO) Nanomaterials for Biomedical Applications: A Review. *JPhys Mater.* **2020**, *3*, 034005. [CrossRef]
22. Rabiee, N. *Green Synthesized Nanomaterials: Principles, Progress, and Perspectives*; American Chemical Society: Washington, DC, USA, 2025; pp. 1–27. [CrossRef]
23. Sidorowicz, A.; Fais, G.; Desogus, F.; Loy, F.; Licheri, R.; Lai, N.; Cao, G.; Concas, A. Eco-Friendly Photocatalytic Treatment of Dyes with Ag Nanoparticles Obtained through Sustainable Process Involving Spirulina Platensis. *Sustainability* **2024**, *16*, 8758. [CrossRef]
24. Sidorowicz, A.; Fais, G.; Desogus, F.; Loy, F.; Licheri, R.; Lai, N.; Locci, A.M.; Cincotti, A.; Orrù, R.; Cao, G.; et al. Optimization of Brilliant Blue R Photocatalytic Degradation by Silver Nanoparticles Synthesized Using Chlorella Vulgaris. *Environ. Sci. Pollut. Res.* **2024**, *31*, 57765–57777. [CrossRef]
25. Fais, G.; Ghiani, F.; Dessì, D.; Casula, M.; Perra, G.; Torchia, E.; Lai, N.; Cao, G.; Concas, A. Superfood Potential of Chlorella Vulgaris: Productivity and Antioxidant Boost under Simulated Moon and Microgravity Conditions. *NPJ Microgravity* **2026**, *12*, 8. [CrossRef]
26. Sidorowicz, A.; Fais, G.; Casula, M.; Borselli, M.; Giannaccare, G.; Locci, A.M.; Lai, N.; Orrù, R.; Cao, G.; Concas, A. Nanoparticles from Microalgae and Their Biomedical Applications. *Mar. Drugs* **2023**, *21*, 352. [CrossRef]
27. Naganthran, A.; Verasoundarapandian, G.; Khalid, F.E.; Masarudin, M.J.; Zulkharnain, A.; Nawawi, N.M.; Karim, M.; Abdullah, C.A.C.; Ahmad, S.A. Synthesis, Characterization and Biomedical Application of Silver Nanoparticles. *Materials* **2022**, *15*, 427. [CrossRef]
28. Braga, M.Q.; Lorentz, J.F.; Pereira, A.S.A.d.P.; Magalhães, I.B.; Silva, T.A.; Avelar, N.V.; Henriques, B.S.; Castro, A.P.M.d.; Assemany, P.P.; Calijuri, M.L. Application of Nanoparticles to Microalgae-Based Wastewater Treatment: Mechanisms, Bioremediation Potential and Technological Frontiers. *J. Environ. Manag.* **2026**, *401*, 128827. [CrossRef]
29. Mirsadeghi, S.; Zandavar, H.; Sahebi, H.; Pourmortazavi, S.M. Holistic Assessment of a Photocatalytic Nanocomposite for Pharmaceutical Wastewater Treatment: Integrating Thermodynamic, Economic, and Environmental Indicators. *Sustain. Energy Technol. Assess.* **2026**, *86*, 104827. [CrossRef]
30. Huerta-Aguilar, C.A.; Palos-Barba, V.; Thangarasu, P.; Koodali, R.T. Visible Light Driven Photo-Degradation of Congo Red by TiO2–ZnO/Ag: DFT Approach on Synergetic Effect on Band Gap Energy. *Chemosphere* **2018**, *213*, 481–497. [CrossRef]
31. Sugiura, E.; Furukawa, M.; Tateishi, I.; Katsumata, H.; Kaneco, S. Development of Ag/Ag2O/ZnO Photocatalyst and Their Photocatalytic Activity towards Dibutyl Phthalate Decomposition in Water. *J. Air Waste Manage. Assoc.* **2022**, *72*, 1137–1152. [CrossRef]

32. Chong, M.N.; Jin, B.; Chow, C.W.K.; Saint, C. Recent Developments in Photocatalytic Water Treatment Technology: A Review. *Water Res.* **2010**, *44*, 2997–3027. [CrossRef]
33. Fais, G.; Sidorowicz, A.; Perra, G.; Dessì, D.; Loy, F.; Lai, N.; Follesa, P.; Orrù, R.; Cao, G.; Concas, A. Cytotoxic Effects of ZnO and Ag Nanoparticles Synthesized in Microalgae Extracts on PC12 Cells. *Mar. Drugs* **2024**, *22*, 549. [CrossRef] [PubMed]
34. Folch, J.; Lees, M.; Sloane, G.H. A Simple Method for the Isolation and Purification of Total Lipides from Animal Tissues. *J. Biol. Chem.* **1957**, *226*, 497–509. [CrossRef]
35. Landi, S.; Segundo, I.R.; Freitas, E.; Vasilevskiy, M.; Carneiro, J.; Tavares, C.J. Use and Misuse of the Kubelka-Munk Function to Obtain the Band Gap Energy from Diffuse Reflectance Measurements. *Solid State Commun.* **2022**, *341*, 114573. [CrossRef]
36. Josun, J.; Sharma, P.; Kumar Garg, V. Optical and Structural Behavior of Hydrothermally Synthesized ZnO Nanoparticles at Various Temperatures with NaOH Molar Ratios. *Results Opt.* **2024**, *14*, 100601. [CrossRef]
37. Coulter, J.B.; Birnie, D.P. Assessing Tauc Plot Slope Quantification: ZnO Thin Films as a Model System. *Phys. Status Solidi B Basic Res.* **2018**, *255*, 1700393. [CrossRef]
38. Busila, M.; Musat, V.; Alexandru, P.; Romanitan, C.; Brincoveanu, O.; Tucureanu, V.; Mihalache, I.; Iancu, A.V.; Dediu, V. Antibacterial and Photocatalytic Activity of ZnO/Au and ZnO/Ag Nanocomposites. *Int. J. Mol. Sci.* **2023**, *24*, 16939. [CrossRef]
39. Zhong, H.; Pan, F.; Yue, S.; Qin, C.; Hadjiev, V.; Tian, F.; Liu, X.; Lin, F.; Wang, Z.; Bao, J. Idealizing Tauc Plot for Accurate Bandgap Determination of Semiconductor with Ultraviolet-Visible Spectroscopy: A Case Study for Cubic Boron Arsenide. *J. Phys. Chem. Lett.* **2023**, *14*, 6702–6708. [CrossRef]
40. Norouzzadeh, P.; Mabhouti, K.; Golzan, M.M.; Naderali, R. Consequence of Mn and Ni Doping on Structural, Optical and Magnetic Characteristics of ZnO Nanopowders: The Williamson–Hall Method, the Kramers–Kronig Approach and Magnetic Interactions. *Appl. Phys. A Mater. Sci. Process.* **2020**, *126*, 154. [CrossRef]
41. Kaiser, C.; Sandberg, O.J.; Zarrabi, N.; Li, W.; Meredith, P.; Armin, A. A Universal Urbach Rule for Disordered Organic Semiconductors. *Nat. Commun.* **2021**, *12*, 3988. [CrossRef]
42. Marchelek, M.; Diak, M.; Kozak, M.; Zaleska-Medynska, A.; Grabowska, E. Some Unitary, Binary, and Ternary Non-TiO2 Photocatalysts. In *Semiconductor Photocatalysis—Materials, Mechanisms and Applications*; InTech: Nappanee, IN, USA, 2016.
43. Sharwani, A.A.; Narayanan, K.B.; Khan, M.E.; Han, S.S. Photocatalytic Degradation Activity of Goji Berry Extract Synthesized Silver-Loaded Mesoporous Zinc Oxide (Ag@ZnO) Nanocomposites under Simulated Solar Light Irradiation. *Sci. Rep.* **2022**, *12*, 10017. [CrossRef]
44. Querebillo, C.J. A Review on Nano Ti-Based Oxides for Dark and Photocatalysis: From Photoinduced Processes to Bioimplant Applications. *Nanomaterials* **2023**, *13*, 982. [CrossRef]
45. Liu, X.; Li, W.; Chen, N.; Xing, X.; Dong, C.; Wang, Y. Ag-ZnO Heterostructure Nanoparticles with Plasmon-Enhanced Catalytic Degradation for Congo Red under Visible Light. *RSC Adv.* **2015**, *5*, 34456–34465. [CrossRef]
46. Atzori, F.; Cosenza, B.; Zedda, F.; Sidorowicz, A.; Fais, G.; Cao, G.; Concas, A. Hybrid Modeling of Photocatalytic Contaminant Degradation Using Nanomaterials Synthesized with Microalgal Extracts. *Chem. Eng. Sci.* **2025**, *316*, 121945. [CrossRef]
47. Zhou, H.; Qiu, Y.; Yang, C.; Zang, J.; Song, Z.; Yang, T.; Li, J.; Fan, Y.; Dang, F.; Wang, W. Efficient Degradation of Congo Red in Water by UV-Vis Driven CoMoO4/PDS Photo-Fenton System. *Molecules* **2022**, *27*, 8642. [CrossRef]
48. Bhagwat, U.O.; Wu, J.J.; Asiri, A.M.; Anandan, S. Photocatalytic Degradation of Congo Red Using PbTiO3 Nanorods Synthesized via a Sonochemical Approach. *ChemistrySelect* **2018**, *3*, 11851–11858. [CrossRef]
49. Tran, H.D.; Nguyen, D.Q.; Do, P.T.; Tran, U.N.P. Kinetics of Photocatalytic Degradation of Organic Compounds: A Mini-Review and New Approach. *RSC Adv.* **2023**, *13*, 16915–16925. [CrossRef]
50. Ranjbari, A.; Adhikary, K.K.; Kashif, M.; Anbari, A.P.; Siddhartha, T.R.; Kim, D.; Yoon, S.; Yoon, J.; Heynderickx, P.M. Comparative Photocatalytic Degradation of Cationic Rhodamine B and Anionic Bromocresol Green Using Reduced ZnO: A Detailed Kinetic Modeling Approach. *Chemosphere* **2025**, *371*, 144052. [CrossRef] [PubMed]
51. Rasoulifard, M.H.; Seyed Dorraji, M.S.; Amani-Ghadim, A.R.; Keshavarz-Babaeinezhad, N. Visible-Light Photocatalytic Activity of Chitosan/Polyaniline/CdS Nanocomposite: Kinetic Studies and Artificial Neural Network Modeling. *Appl. Catal. A Gen.* **2016**, *514*, 60–70. [CrossRef]
52. Zhan, X.; Yan, C.; Zhang, Y.; Rinke, G.; Rabsch, G.; Klumpp, M.; Schäfer, A.I.; Dittmeyer, R. Investigation of the Reaction Kinetics of Photocatalytic Pollutant Degradation under Defined Conditions with Inkjet-Printed TiO2films-from Batch to a Novel Continuous-Flow Microreactor. *React. Chem. Eng.* **2020**, *5*, 1658–1670. [CrossRef]
53. Sidorowicz, A.; Atzori, F.; Zedda, F.; Fais, G.; Loy, F.; Licheri, R.; Lai, N.; Desogus, F.; Cao, G.; Concas, A. Novel Experimental and Theoretical Study on the Synthesis and Use of Microalgae-Derived Silver Nanomaterials for Water Purification. *J. Water Process Eng.* **2025**, *69*, 106831. [CrossRef]
54. Du, B.; Li, Y.; Li, Y.; Xie, C.; Wang, X.; Zhu, W.; Yang, Y.; You, L.; Zhang, L.; Zhao, B. Modeling of PEMEL Hydrogen Production Systems: Comprehensive Multivariate Sensitivity Analysis Considering Mass-Energy Dynamic Equilibrium. *Appl. Energy* **2025**, *377*, 124644. [CrossRef]
55. Mitra, A. The Taguchi Method. *Wiley Interdiscip. Rev. Comput. Stat.* **2011**, *3*, 472–480. [CrossRef]

56. Antony, J. Taguchi or Classical Design of Experiments: A Perspective from a Practitioner. *Sens. Rev.* **2006**, *26*, 227–230. [CrossRef]
57. Wu, H.; Li, H.; Wang, X.; Yang, J.; Jiang, R.; Deng, X.; Wang, J. Research on Multi-Objective Optimization Design for High-Precision Turning-Milling Machine Tool Bed Based on Taguchi Method -FEA. *Sci. Rep.* **2025**, *15*, 27307. [CrossRef]
58. Bindu, P.; Thomas, S. Estimation of Lattice Strain in ZnO Nanoparticles: X-Ray Peak Profile Analysis. *J. Theor. Appl. Phys.* **2014**, *8*, 123–134. [CrossRef]
59. Vinitha, V.; Preeyanghaa, M.; Anbarasu, M.; Jeya, G.; Neppolian, B.; Sivamurugan, V. Aminolytic Depolymerization of Polyethylene Terephthalate Wastes Using Sn-Doped ZnO Nanoparticles. *J. Polym. Environ.* **2022**, *30*, 3566–3581. [CrossRef]
60. Kondratenko, T.; Ovchinnikov, O.; Grevtseva, I.; Smirnov, M.; Erina, O.; Khokhlov, V.; Darinsky, B.; Tatianina, E. Thioglycolic Acid Ftir Spectra on Ag2S Quantum Dots Interfaces. *Materials* **2020**, *13*, 909. [CrossRef] [PubMed]
61. Vivek, C.; Balraj, B.; Thangavel, S. Structural, Optical and Electrical Behavior of ZnO@Ag Core–Shell Nanocomposite Synthesized via Novel Plasmon-Green Mediated Approach. *J. Mater. Sci. Mater. Electron.* **2019**, *30*, 11220–11230. [CrossRef]
62. Shaban, A.S.; Owda, M.E.; Basuoni, M.M.; Mousa, M.A.; Radwan, A.A.; Saleh, A.K. Punica Granatum Peel Extract Mediated Green Synthesis of Zinc Oxide Nanoparticles: Structure and Evaluation of Their Biological Applications. *Biomass Convers. Biorefin.* **2024**, *14*, 12265–12281. [CrossRef]
63. Dhawale, S.K.; Sarvalkar, P.D.; Shinde, C.S.; Prasad, N.R.; Garadkar, K.M.; Sharma, K.K.K.; Ramteke, A.A. Studies on Photocatalytic and Antioxidant Efficacy of Ag-Embedded ZnO Nanocomposites. *ACS Omega* **2025**, *10*, 11948–11960. [CrossRef]
64. Sampaio, M.J.; Lima, M.J.; Baptista, D.L.; Silva, A.M.T.; Silva, C.G.; Faria, J.L. Ag-Loaded ZnO Materials for Photocatalytic Water Treatment. *Chem. Eng. J.* **2017**, *318*, 95–102. [CrossRef]
65. Hussain, A.; Fiaz, S.; Almohammedi, A.; Waqar, A. Optimizing Photocatalytic Performance with AG-Doped ZNO Nanoparticles: Synthesis and Characterization. *Heliyon* **2024**, *10*, e35725. [CrossRef]
66. Georgekutty, R.; Seery, M.K.; Pillai, S.C. A Highly Efficient Ag-ZnO Photocatalyst: Synthesis, Properties, and Mechanism. *J. Phys. Chem. C* **2008**, *112*, 13563–13570. [CrossRef]
67. Nie, M.; Liao, J.; Cai, H.; Sun, H.; Xue, Z.; Guo, P.; Wu, M. Photocatalytic Property of Silver Enhanced Ag/ZnO Composite Catalyst. *Chem. Phys. Lett.* **2021**, *768*, 138394. [CrossRef]
68. Vadakkan, K.; Rumjit, N.P.; Ngangbam, A.K.; Vijayanand, S.; Nedumpillil, N.K. Novel Advancements in the Sustainable Green Synthesis Approach of Silver Nanoparticles (AgNPs) for Antibacterial Therapeutic Applications. *Coord. Chem. Rev.* **2024**, *499*, 215528. [CrossRef]
69. Rizwan, M.; Amin, S.; Kudaibergenova, B.M.; Rauf, A.; Siddique, M.; Ullah, K.; Bawazeer, S.; Farooq, U.; Mabkhot, Y.N.; Ramadan, M.F. Green Synthesis and Antimicrobial Potential of Silver Nanoparticles with Boerhavia Procumbens Extract. *J. Pure Appl. Microbiol.* **2020**, *14*, 1437–1451. [CrossRef]
70. Anum, F.; Jabeen, K.; Javad, S.; Iqbal, S.; Tahir, A.; Javed, Z.; Cruz-Martins, N.; Ayatollahi, S.A.; Sharifi-Rad, J.; Alshehri, M.M.; et al. Green Synthesized Silver Nanoparticles as Potent Antifungal Agent against Aspergillus Terreus Thom. *J. Nanomater.* **2021**, *2021*. [CrossRef]
71. Sidorowicz, A.; Szymański, T.; Rybka, J.D. Photodegradation of Biohazardous Dye Brilliant Blue r Using Organometallic Silver Nanoparticles Synthesized through a Green Chemistry Method. *Biology* **2021**, *10*, 784. [CrossRef] [PubMed]
72. Aspoukeh, P.K.; Barzinjy, A.A.; Hamad, S.M. A Novel Approach to the Green Synthesis of Zinc Oxide Nanorods Using Thymus Kotschyanus Plant Extract: Effect of Ammonium Hydroxide and Precursor Concentration. *Nano Express* **2023**, *4*, 045001. [CrossRef]
73. Sidorowicz, A.; Yigit, N.; Wicht, T.; Stöger-Pollach, M.; Concas, A.; Orrù, R.; Cao, G.; Rupprechter, G. Microalgae-Derived Co3O4 Nanomaterials for Catalytic CO Oxidation. *RSC Adv.* **2024**, *14*, 4575–4586. [CrossRef]
74. Fouad, S.S.; Soliman, L.I.; Baradács, E.; Osman, N.F.; Nabil, M.; Sayed, M.E.; Tomán, J.J.; Mehta, N.; Erdélyi, Z. Comparative Insights into Structural and Optical Properties of ZnO/Ag/ZnO and Ag/ZnO/Ag Ternary Layer Thin Films. *Nanoscale Adv.* **2025**, *7*, 7811–7825. [CrossRef]
75. Baig, A.; Siddique, M.; Panchal, S. A Review of Visible-Light-Active Zinc Oxide Photocatalysts for Environmental Application. *Catalysts* **2025**, *15*, 100. [CrossRef]
76. Mangala Nagasundari, S.; Muthu, K.; Kaviyarasu, K.; Farraj, D.A.A.; Alkufeidy, R.M. Current Trends of Silver Doped Zinc Oxide Nanowires Photocatalytic Degradation for Energy and Environmental Application. *Surf. Interfaces* **2021**, *23*, 100931. [CrossRef]
77. Alzahrani, E.A.; Nabi, A.; Kamli, M.R.; Albukhari, S.M.; Althabaiti, S.A.; Al-Harbi, S.A.; Khan, I.; Malik, M.A. Facile Green Synthesis of ZnO NPs and Plasmonic Ag-Supported ZnO Nanocomposite for Photocatalytic Degradation of Methylene Blue. *Water* **2023**, *15*, 384. [CrossRef]
78. Makuła, P.; Pacia, M.; Macyk, W. How To Correctly Determine the Band Gap Energy of Modified Semiconductor Photocatalysts Based on UV-Vis Spectra. *J. Phys. Chem. Lett.* **2018**, *9*, 6814–6817. [CrossRef]
79. Kopach, V.R.; Klepikova, K.S.; Klochko, N.P.; Tyukhov, I.I.; Khrypunov, G.S.; Korsun, V.E.; Lyubov, V.M.; Kopach, A.V.; Zaitsev, R.V.; Kirichenko, M.V. Solar Active Ag/ZnO Nanostructured Arrays Obtained by a Combination of Electrochemical and Chemical Methods. *Sol. Energy* **2016**, *136*, 23–31. [CrossRef]

80. Pandey, P.K.; Chauhan, V.; Dixit, P.; Pandey, P.C. Correlation of Enhanced Photocurrent with Structural and Optical Properties of Ag–ZnO Nanocomposites Synthesized by a Facile Chemical Route. *Phys. B Condens. Matter* **2021**, *612*, 412937. [CrossRef]
81. Svoboda, L.; Vilamová, Z.; Praus, P.; Novák, V.; Mamulová Kutláková, K.; Petr, M.; Bednář, J.; Jochim, V.; Šimonová, Z.; Dvorský, R. Optimization of the Urbach Energy and Charge Carrier Dynamics in G-C3N4 through Strategic Potassium Precursor Selection: Insights and Challenges. *Appl. Surf. Sci.* **2025**, *679*, 161162. [CrossRef]
82. Güy, N.; Özacar, M. The Influence of Noble Metals on Photocatalytic Activity of ZnO for Congo Red Degradation. *Int. J. Hydrogen Energy* **2016**, *41*, 20100–20112. [CrossRef]
83. Su, Y.; Zhao, X.; Bi, Y.; Han, X. ZnO/Ag–Ag2O Microstructures for High-Performance Photocatalytic Degradation of Organic Pollutants. *Clean Technol. Environ. Policy* **2019**, *21*, 367–378. [CrossRef]
84. Farbod, M.; Sharif, L.; Ahangarpour, A. A Novel Synthesis of Ag@ZnO Yolk-Shell and ZnO Hollow Sphere Nanostructures and Comparison of Their Photocatalytic Performances. *Phys. B Condens. Matter* **2021**, *613*, 412729. [CrossRef]
85. Tanuj; Sharma, A.; Kumar, R.; Kumar, S.; Kalra, N. Unleashing the Potential of Vitex Negundo Leaves: Innovative Fabrication of Cu-Ag-ZnO Nanocomposite for Enhanced Photocatalytic Degradation of Caffeine and Congo Red Dye Coupled with Antimicrobial Efficacy. *Biomass Convers. Biorefinery* **2025**, *15*, 23423–23440. [CrossRef]
86. Sanyal, A.; Krishna, P.G.; Johnson, V.; Sukumar, U.K. Mechanistic Insights into Photoactive Interfaces of Mesoporous Ag–ZnO Nanohybrids for Mitigation of Recalcitrant Organic Pollutants. *Appl. Surf. Sci.* **2026**, *723*, 165618. [CrossRef]
87. Jo, Y.J.; Patil, R.P.; Chae, W.S.; Kim, H.G.; Choi, S.H.; Jang, J.S. Template-Assisted Synthesis of Porous Ag/ZnO Photocatalyst from ZnS(HDA)0.5/ZnO for Enhanced Degradation of Organic Pollutants and Bacterial Inactivation. *Colloids Surf. A Physicochem. Eng. Asp.* **2025**, *727*, 138077. [CrossRef]
88. Hamza, L.; Laouini, S.E.; Mohammed, H.A.; Meneceur, S.; Salmi, C.; Alharthi, F.; Legmairi, S.; Abdullah, J.A.A. Biosynthesis of ZnO/Ag Nanocomposites Heterostructure for Efficient Photocatalytic Degradation of Antibiotics and Synthetic Dyes. *Z. Fur Phys. Chem.* **2024**, *238*, 1599–1622. [CrossRef]
89. Dumbrava, A.; Matei, C.; Diacon, A.; Moscalu, F.; Ziko, L.; Sedky, N.K.; Berger, D. Ag-ZnO Nanocomposites with Photocatalytic and Antimicrobial Properties Obtained by Green Synthesis in Ulva Lactuca Aqueous Extract. *J. Appl. Phycol.* **2026**. [CrossRef]
90. Georgin, J.; Ramos, C.G.; de Oliveira, J.S.; Dehmani, Y.; El Messaoudi, N.; Meili, L.; Franco, D.S.P. A Critical Review of the Advances and Current Status of the Application of Adsorption in the Remediation of Micropollutants and Dyes Through the Use of Emerging Bio-Based Nanocomposites. *Sustainability* **2025**, *17*, 2012. [CrossRef]
91. Herrmann, J.-M. Heterogeneous Photocatalysis: Fundamentals and Applications to the Removal of Various Types of Aqueous Pollutants. *Catal. Today* **1999**, *53*, 115–129. [CrossRef]
92. Belhamra, F.; Temam, E.G.; Rahmane, S.; Althamthami, M.; NadjetteBelhamra. Enhanced Photocatalytic and Self-Cleaning Performance of Ag2O-Photodeposited ZnO Thin Films Synthesized via Sol-Gel Method for Wastewater Treatment Applications. *J. Solgel Sci. Technol.* **2025**, *116*, 2111–2127. [CrossRef]
93. Aminghafari, M.; Cheze, N.; Poggi, J.M. Multivariate Denoising Using Wavelets and Principal Component Analysis. *Comput. Stat. Data Anal.* **2006**, *50*, 2381–2398. [CrossRef]

https://doi.org/10.3390/su18094607